TICRA

Electromagnetic properties of the ALMA antenna. Front-end analysis.

Author: Stig Busk Sørensen
Erik Jørgensen

September, 2007 S-1430-02

TICRA
LÆDERSTRÆDE 34 · DK-1201 COPENHAGEN K DENMARK
TELEPHONE +45 33 12 45 72 TELEFAX +45 33 12 08 80
E-MAIL ticra@ticra.com http://www.ticra.com

VAT REGISTRATION NO. DK-1055 8697
TICRA FOND, CVR REG. NO. 1055 8697

TABLE OF CONTENTS

1. Introduction

.....

2. Nominal antenna geometry

.....

3. Subreflector

.....

4. Set-up of front ends

This section describes the set up of the ALMA front-end systems in GRASP. The geometry for each of the 10 bands is converted to GRASP format in order to enable a detailed analysis by Physical Optics. This work was facilitated by the QUAST software which is a quasioptical add-on package to GRASP by which the geometry can be specified in terms of the Gaussian-beam data used in the ALMA project. The input data has been found in the Front-end Optics report [1] and in the appendices [2] [3] [4] [5] [6] [7] [8]. It has been checked that the data in these reports are consistent, which they are, except some minor differences.

4.1 Band 1

The Band 1 front-end system consists of a corrugated horn with a focusing dielectric lens mounted some distance in front of the horn aperture. A schematic drawing is shown in Figure 4-1 and a 3D-drwaing in Figure 4-2.

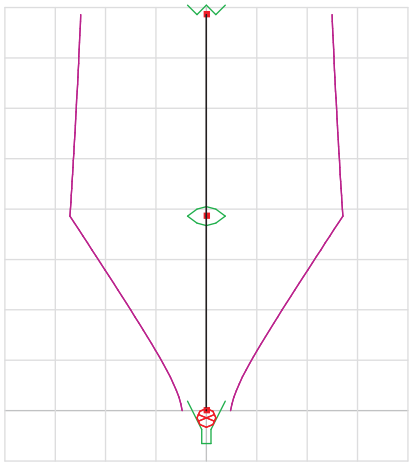

Figure 4-1 Schematic drawing of Band 1. A beam of width $5w$ is shown, corresponding to $-54.3dB$. Grid spacing $= 50mm$

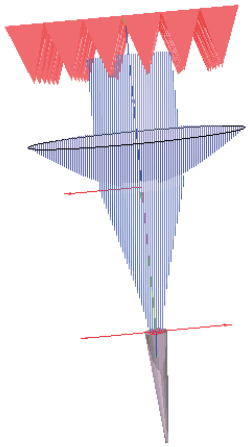

Figure 4-2 3D drawing of Band 1 38 GHz. A beam of radius w is shown, corresponding to $-8.68dB$.

In this figure the lens has a diameter of $5w$ as specified as a goal in [1], Section 2.2. This gives, at the centre frequency, a lens diameter of $5w = 271mm$ which is larger than the specified diameter of $186mm$. In the drawing above, the lens is bi-hyperbolic with curvatures that perfectly matches the wavefront curvatures at the centre frequency. The index of refraction is $n = 1.5$.

In [2] the corrugated horn and the lens are specified, but more details and information about the position of the horn and lens is neccesary for a complete GRASP analysis. Consequently, the front end will be represented by a simple Gaussian beam model in the GRASP analysis.

4.2 Band 2

The Band 2 front-end system is similar to Band 1 and consists of a corrugated horn and a focusing dielectric lens. A schematic drawing is shown in Figure 4-3 and a 3D-drwaing in Figure 4-4, where the lens diameter is $5w$.

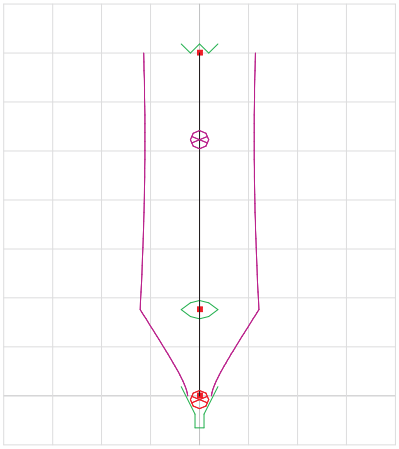

Figure 4-3 Schematic drawing of Band 2. A beam of width $5w$ is shown, corresponding to $-54.3dB$. Grid spacing $= 50mm$

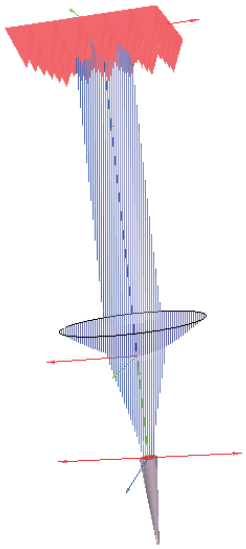

Figure 4-4 3D drawing of Band 2 at 78 GHz. A beam of radius w is shown, corresponding to $-8.68dB$.

In the drawing above, the lens is assumed to be bi-hyperbolic with curvatures that perfectly matches the wavefront curvatures at the centre frequency. The index of refraction is 1.5.

In [3] the corrugated horn and the lens are specified, but more details and information about the position of the horn and lens is

neccesary for a complete GRASP analysis. Consequently, the front end will be represented by a simple Gaussian beam model in the GRASP analysis.

4.3 Band 3

Band 3 consists of a corrugated horn and two mirrors. The first mirror (seen from the feed) is ellipsoidal and the second is planar. The system is redefined in [1] compared to previous reports in the way that there is now a lens mounted in the aperture of the horn, designed such that a waist is generated just in front of the lens.

A schematic drawing of the Band 3 front-end system is shown in Figure 4-5 and a 3D-drwaing in Figure 4-6. The mirrors in 4-5 are just symbolic, whereas the mirror diameters in 4-6 correspond to $5w$.

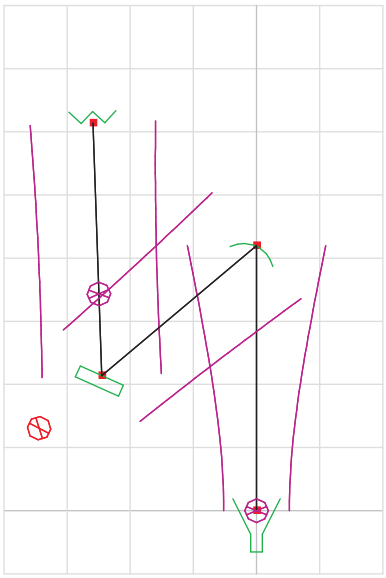

Figure 4-5 Schematic drawing of Band 3. A beam of width $5w$ is shown, corresponding to $-54.3dB$. Grid spacing $= 50mm$

4.3.1 Feed geometry and analysis

The feed is defined in the drawing shown in Figure 4-7.

It is found:

Axial length:	$40.9000 + 3.0/(2 \cdot \tan 18.0°) = 45.5165$ mm
Aperture diameter:	$D =$Axial length$\cdot 2 \tan 18.0° = 29.5784$ mm
Slant Length:	Axial length$/\cos 18.0° = 47.8589$ mm

where it has been used that the waveguide diameter according to the drawing is 3.00 mm.

A simple hybrid-mode model for the horn radiation will be used in the GRASP analysis. In order to validate this model the horn was analysed with Ticra's mode-matching software CHAMP as shown

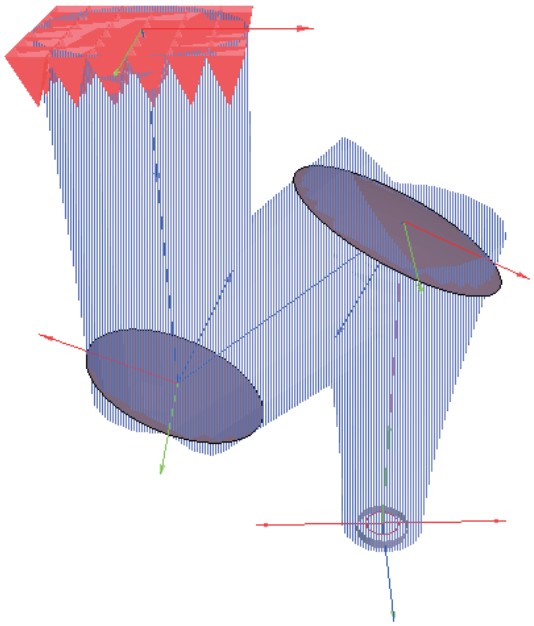

Figure 4-6 3D drawing of Band 3 at 100 GHz. A beam of radius $5w$ is shown, corresponding to $-54.3dB$.

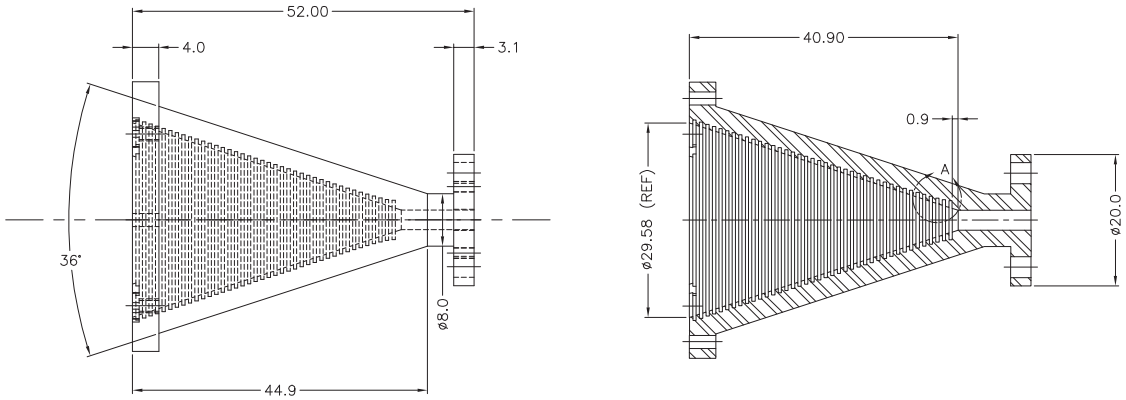

Figure 4-7 Band 3 feed geometry, from [4], p.69

in Figure 4-8. The hybrid-mode model is not able to predict cross polarisation, but the agreement in the co-polar field at 100 GHz is very good. At 115 GHz the mode-matching calculations give a high cross-polar field and different co-polar patterns in the E- and H-planes. This does not agree well with the hybrid-mode model and indicates that the corrugated horn is not well designed for this frequency as confirmed by the meassurements in [4], p.9. Analysis at other frequencies show an excellent agreement between the mode-matching and hybrid-mode models and also good agreement with the measurements (except at 92 GHz, at which there seems to be an error in the measurements). Because of the horn problem at 115 GHz the CHAMP data will be used for the final antenna analysis.

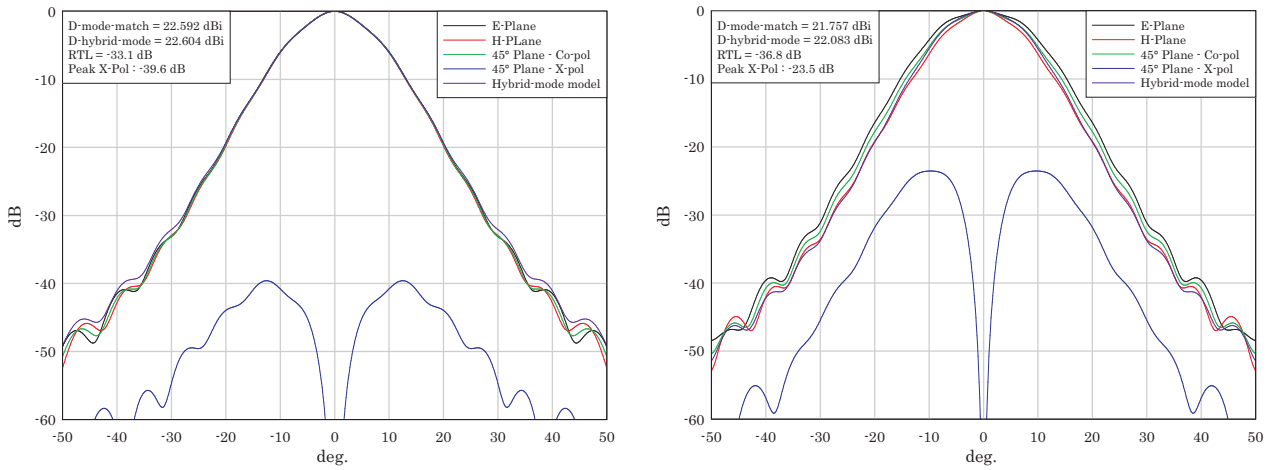

Figure 4-8 Band 3 feed patterns. Comparison between mode-matching and hybrid-mode model. Left figure: 100 GHz. Right figure: 115 GHz.

4.3.2 Lens geometry and analysis

The lens is plano-convex with geometry shown in Figure 4-9, from [4], p.70. On this page the shape of the curved face of the lens is defined by an analytic expression and it is noted that the lens material is PTFE with a refractive index of $n = 1.469$.

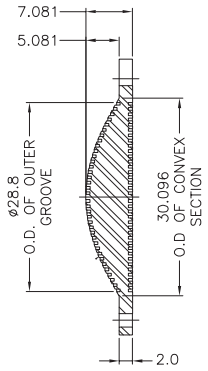

Figure 4-9 Band 3 lens geometry.

The lens has been analysed by 3 methods: Geometrical Optics (GO), Physical Optics (PO) and the Method of Moments (MoM). PO and MoM are in excellent agreement, whereas GO deviates with respect to max. directivity and sidelobe-level (see Figure 4-10). This can probably be attributed to the small size of the lens (10λ). The MoM analysis is time consuming, but in principle exact (except for the coupling with the horn and the grooves in the lens surface) and since it agrees well with the much faster PO, the PO method will be used in the following analysis.

In order to compare the analysis with the measurements in [4], p. 20, a PO lens analysis is shown in Figure 4-11, where the incident

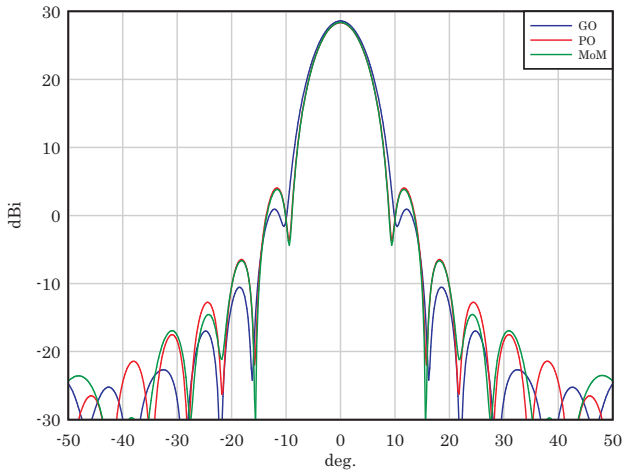

Figure 4-10 Band 3 lens analysis. Comparison of GO, PO and MoM.
E-plane cuts. Frequency: 100 GHz

field from the feed is computed with both the hybrid mode model and CHAMP mode matching. It is seen that the mode matching predicts cx pol. level approximately -40 dB below peak, whereas the cx pol. level in the measurements is -30 dB below peak. An investigation of this requires a detailed modelling of the effects of the grooves in the lens which have not been taken into account in the present analysis, but will be treated in Section 4.3.7.

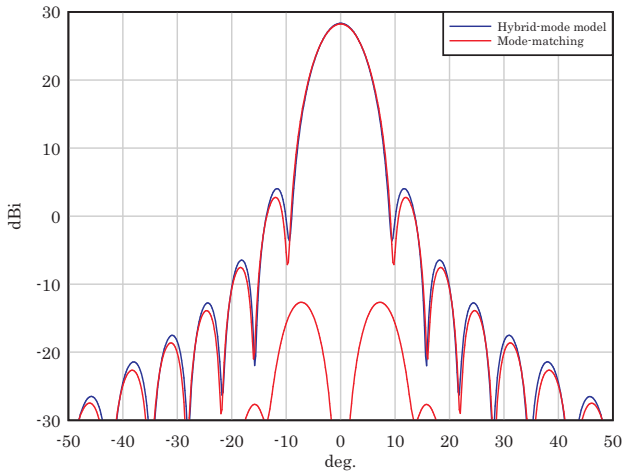

Figure 4-11 Band 3 lens analysis. Comparison of hybrid mode model and mode matching, 100 GHz.
Co pol. in E-plane and cx pol. for $\phi = 45°$ deg.

It is noted that the analytical expression given in [4], p. 70 is not identical to the expression in the handbook [9], p. 16-4, in which an additional term is included. This has the consequence that, according to Gaussian beam analysis, the waist of the beam that comes out of the lens is located $37.9mm$ above the lens instead of just on the upper lens surface as specified in [1] in Table 10, p. 33.

The difference between the two lens shapes is, however, small as shown in Figure 4-12 and the electrical performance is also similar when calculated by PO, see Figure 4-13.

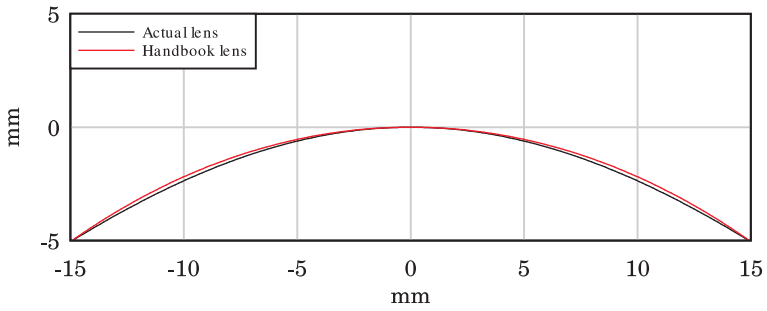

Figure 4-12 Comparison between actual lens design and handbook design.

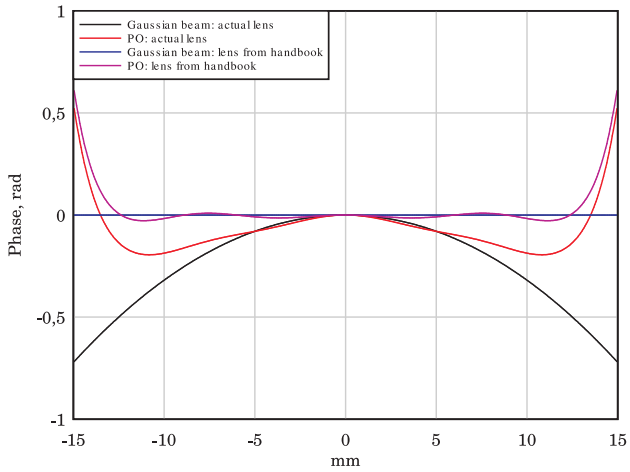

Figure 4-13 Phase of horn+lens in E-plane cut at 100 GHz, just above the upper lens surface.
Gausian beam analysis and PO is compared.

Figure 4-13 can be compared to measurements in [10], p. 19 as shown in Figure 4-14. The PO analysis cannot reproduce the curve to the right in Figure 4-14 where the phase is almost constant. In the PO calculations the H-plane has a phase variation similar to the E-plane, but the difference in the two plots in Figure 4-14 is maybe caused by the grooves, which have not been included in the calculations. The measurements show that the actual lens works well and it is not certain that the handbook design would give any improvement.

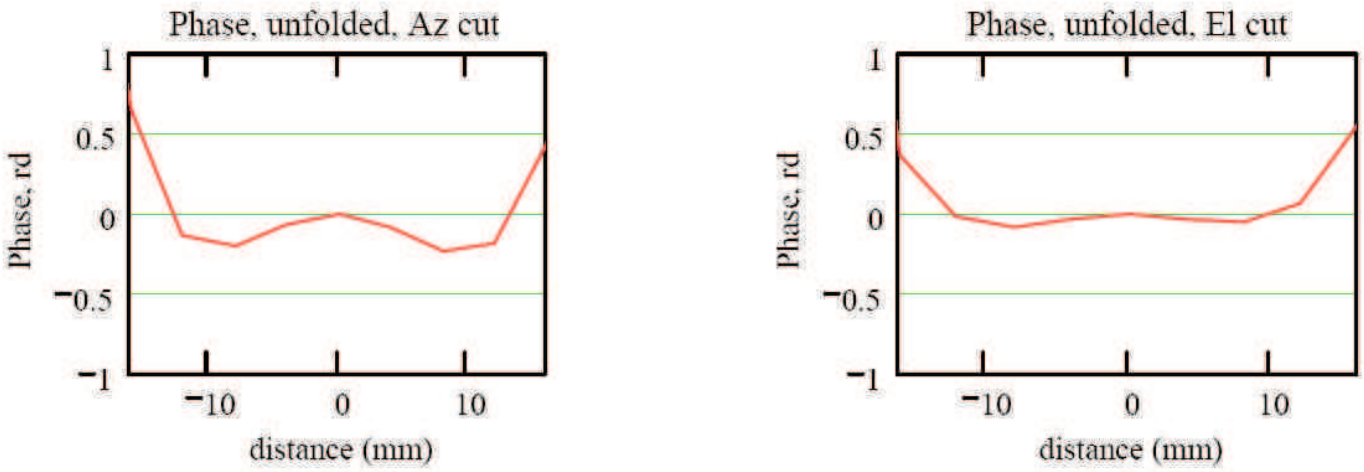

Figure 4-14 Measured phase of horn+lens in two orthogonal cuts at 100 GHz, just above the upper lens surface.
From [10], p. 19.

4.3.3 Mirror 1 geometry

Mirror 1 is an ellipsoid defined by the drawings in Figure 4-15.

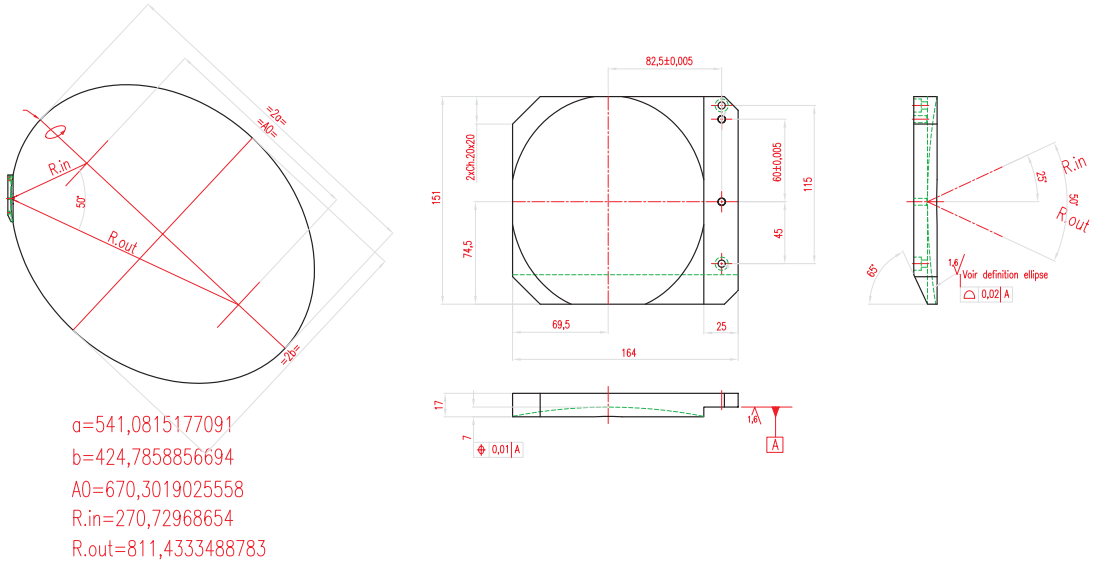

Figure 4-15 Mirror 1 drawing. From [4], p. 74.

If the definition data of the ellipsoid is taken as the half axes a and b from Figure 4-15 and the angle of incidence $\theta_{in} = 25°$ it is possible to derive the other ellipsoid parameters and the focal length which becomes $f = 203.0000$ mm in agreement with Table 10 in [1], p. 33. The rim is also defined in Figure 4-15 where it is indicated that the plane of the rim is parallel to the surface tangent plane in the centre reflection point, and that the distance from this point to the rim plane is 7.0000 mm. From this definition the rim curve

becomes a planar ellipse, but with cut-offs as defined on the drawing. It has been checked that these data are consistent and that they agree with the other data on the drawing.

4.3.4 Mirror 2 geometry

Mirror 2 is planar with dimensions shown in Figure 4-16. According to [4], p. 71 it is located in the distance 160.000 mm from mirror 1 which is sligthly different from the value 160.025 mm given in Table 10 in [1], p. 33. The tilt angle of mirror 2 given in [4], p. 71, results in a beam tilt of 1.8087° which is different from the tilt angle 1.84° in [1], p. 20.

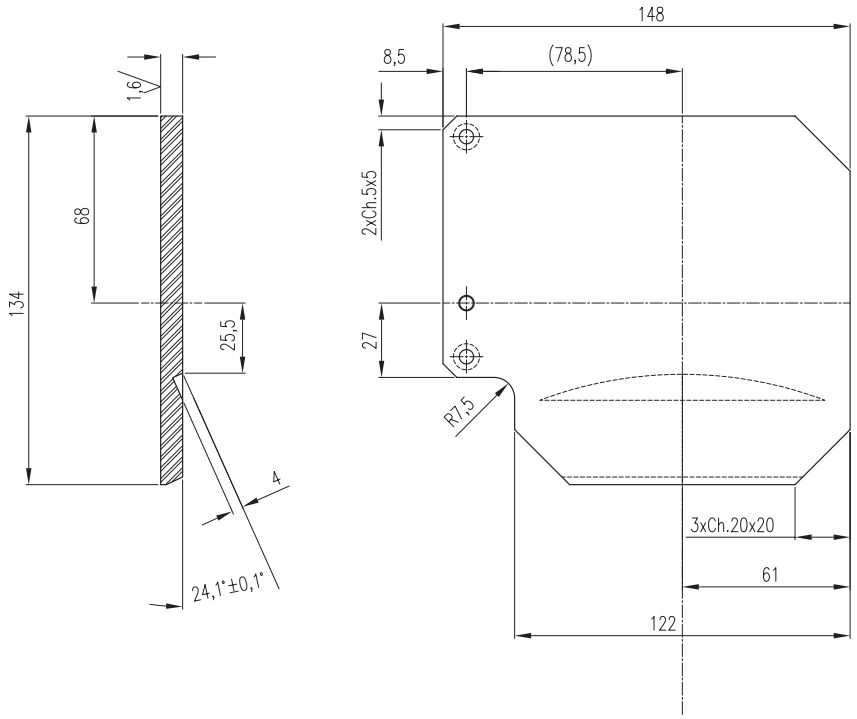

Figure 4-16 Mirror 2 drawing. From [4], p. 75.

4.3.5 Cryostat window and filter geometry

According to [4], p. 71, the cryostat window is located 145.2 mm below the centre reflection point on mirror 1. The information in [11] (as summarized below in Table 4.1) then defines the positions and diameters of the window and filters.

	Cryostat window	110K filter	15K filter
z-coordinate	0	44	57
diameter	70	61	60

Table 4.1 Band 3 cryostat window and filters. z-coordinate and diameter (in mm).

The complete set-up of mirrors and windows is shown in Figure 4-17.

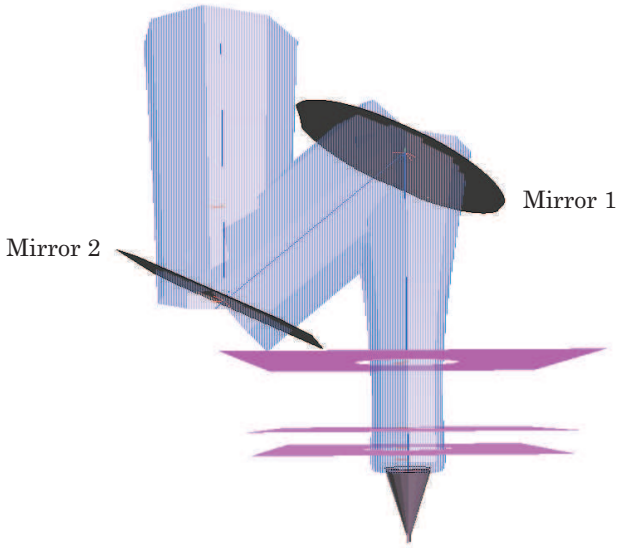

Figure 4-17 Band 3 geometry with mirrors, filters and cryostat window

4.3.6 GRASP analysis results

GRASP analysis of the front end system is presented below. In Figure 4-18 the far field from the mirror system is computed without taking into account the filter and window apertures and the results are compared to an ideal Gaussian beam. For the Band 3 front-end system the ideal output beam has a waist radius of $w_0 = 18.6147$ mm at 100 GHz.

It is seen that there is a significant loss in peak gain which is due to the power in the sidelobes and due to reflection in the lens, which is responsible for a decrease in relative power from 1.0000 to 0.9284 as shown in Table 4.2. The grooves in the lens have not been included in the analysis and will significantly reduce the reflection.

Far-field cuts with and without filter and cryostat apertures are shown in Figure 4-19. The effect of the apertures (without dielectrics) is only significant at levels -40 dB below peak.

A number of scattering effects have been investigated e.g., the direct radiation from the cryostat window and mirror 1 into the far field and the scattering of the output beam from mirror 2 onto mirror 1. Of these effects only the radiation of mirror 2 onto mirror 1 has some significance and is most pronounced at the lower end of the frequency band. A result is shown in Figure 4-20, but the effect is only significant at levels 30 dB below peak.

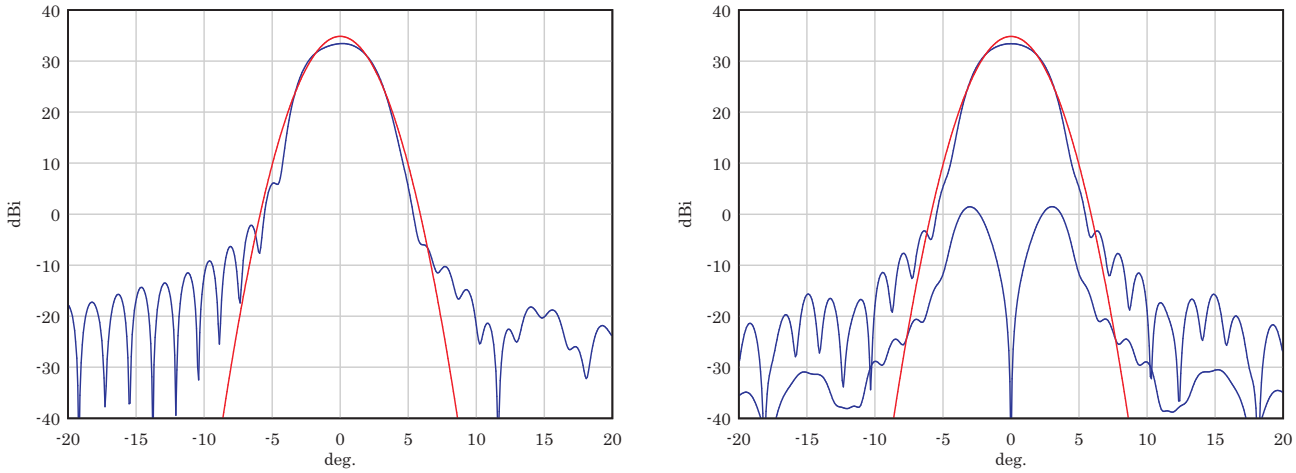

Figure 4-18 Far-field beams for mirror system with hybrid mode feed (blue curves) and ideal Gaussian output beam (red curves). Polarisation along x, i.e. in the plane of symmetry.
Left figure: $\phi = 0°$. Right figure: $\phi = 90°$.
Frequency: 100 GHz

	Relative incident power
15K filter	0.9284
110K filter	0.9282
Cryostat Window	0.9267
Mirror 1	0.9256
Mirror 2	0.9253

Table 4.2 Power loss through lens, apertures and mirrors. Dielectric reflection loss included for lens, but not for apertures.

The largest discrepancy between the design values in [1], Table 10, p. 33, and the actual design is the position of the output beam waist. According to the Gaussian beam analysis in [1] the output waist should be located 64.7678 mm above mirror 2, but with the actual lens design the waist is located app. 65.7 mm below mirror 2. As discussed above, however, both measurements and PO analysis show that the phase of the output beam from the lens is more constant than predicted by Gaussian beam analysis and that the actual lens works well.

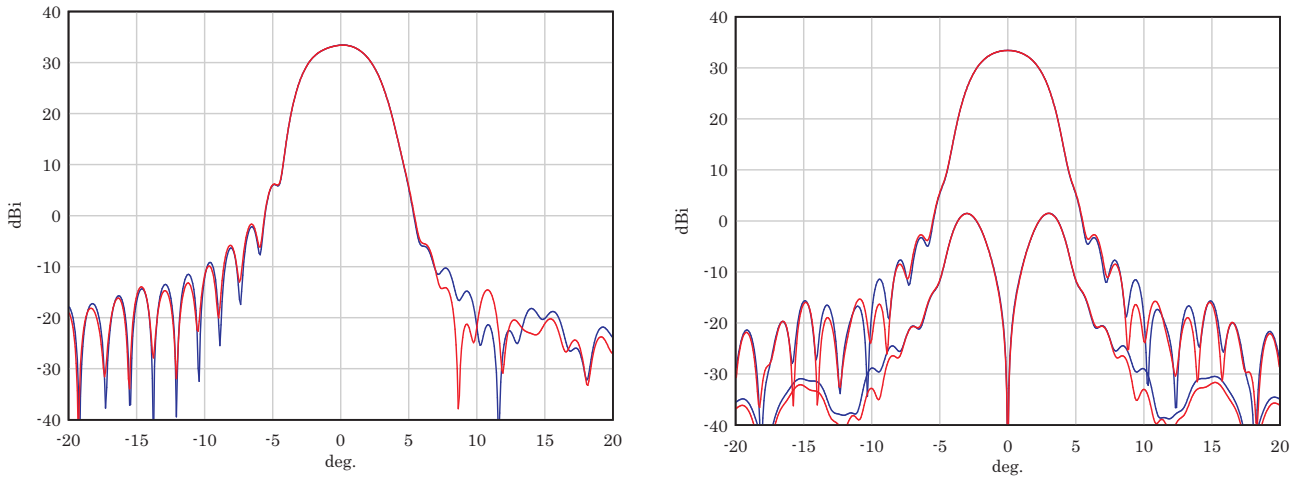

Figure 4-19 Far-field beams for mirror system without apertures (blue curves) and with apertures (red curves). Polarisation along x, i.e. in the plane of symmetry.
Left figure: $\phi = 0°$. Right figure: $\phi = 90°$.
Frequency: 100 GHz

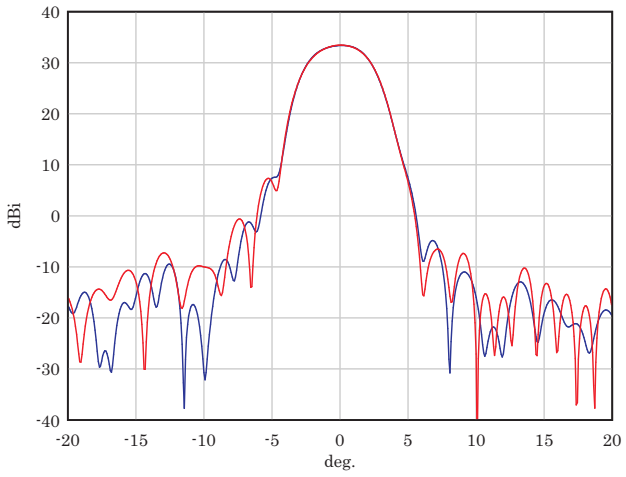

Figure 4-20 Far-field beams for mirror system with apertures (blue curve) and with scattering from mirror 2 onto mirror 1 (red curve). Polarisation along x, i.e. in the plane of symmetry. Cuts for $\phi = 0°$
Frequency: 84 GHz

4.3.7 Accurate Analysis of Grooved Lens

The study of the ALMA front end performance was initially performed with a relatively simple model of the horn-feed combination as described in Section 4.3.2. The horn was modelled with a dedicated corrugated horn software, the horn field was then expanded in terms of plane waves, and the lens was approximated by a smooth lens (without grooves) and analysed by Physical Optics (PO). The accuracy of the PO approximation was checked by running a full Method of Moments (MoM) simulation on a smooth lens and the results showed that PO is sufficiently accurate, even in Band 3, which is the worst case due to the small electrical size of the lens in this band. However, comparisons with the measurements [4] performed on the horn-lens combination revealed that the simple smooth lens model predicted a cross-polarisation approximately 10 dB lower than the actual measured level and it was estimated by IRAM that the grooves improves the peak gain by approximately 0.15 dB. The wrong cross-polar level can be clearly seen in Figure 4-21 that shows the simulated pattern of the smooth lens along with the measured pattern. Due to these differences, it was decided to perform a more accurate study of the effects of the grooves.

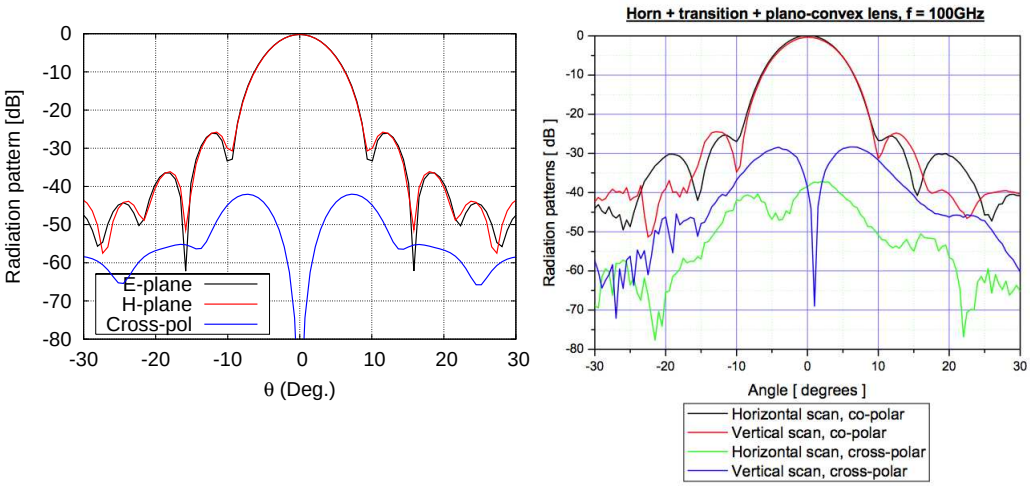

Figure 4-21 Simulated radiation pattern of the smooth lens (left) and measured radiation pattern of the grooved lens (right, reproduced from [4]).

The cross-section of the grooved lens for Band 3 is shown in Figure 4-22. The diameter of the lens is $10.0\lambda_0$, the groove depth is $0.21\lambda_0$, the groove width and the spacing between the grooves are $0.13\lambda_0$, and the relative permittivity is 2.158. The performance of this grooved lens was investigated using the higher-order MoM that has been integrated in GRASP. GRASP was used to compute the radiation patterns of the lens both with and without the grooves. The mesh of the smooth lens employs 348 4th-order quads which

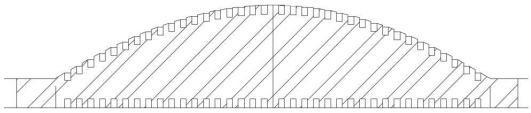

Figure 4-22 Cross-section of grooved plano-convex lens (reproduced from [4]).

were approximately 2 by 2 wavelengths in the dielectric (see Figure 4-23). The large smooth patches calls for a high polynomial order and the maximum polynomial order used in this example is 8 resulting in 24320 unknowns. The mesh of the grooved lens employs 2800 quads and is shown in figure 4-24. The length of the patch edges is anywhere between 0 and 2 wavelengths in the dielectric. The total number of unknowns is 56320 which requires 23 GigaByte of computer memory.

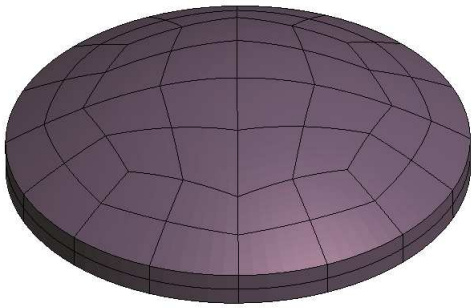

Figure 4-23 Mesh of the smooth lens.

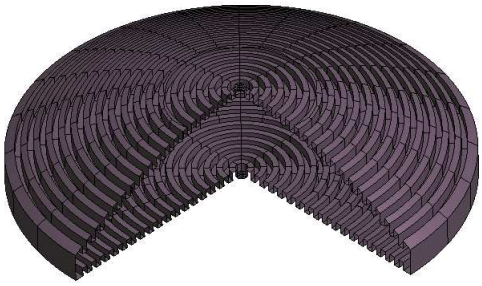

Figure 4-24 Mesh of the grooved lens (one quarter has been removed to show the grooves on the bottom.

The radiation pattern of the horn-lens combination is shown in Figure 4-25. The simulated pattern on the left has improved significantly when compared to the pattern of the smooth lens which was shown in Figure 4-21. The cross-polar level has improved by 10 dB and the side-lobe structure appears to be closer to the measured pattern. Table 4.3 summarizes various parameters for the lens analyses. The power lost by reflection is

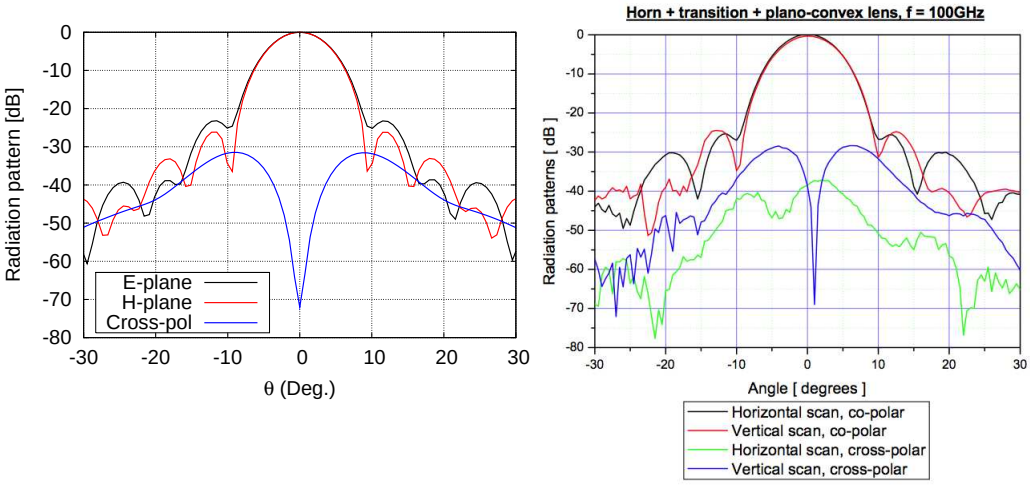

Figure 4-25 Simulated radiation pattern of the grooved lens (left) and measured radiation pattern of the grooved lens (right, reproduced from [4]).

reduced from 0.32 dB (7 percent) to almost nothing when the grooves are introduced. However, the peak co-pol increases only 0.18 dB whereas the remaining power goes into the cross-pol and side lobes. This can be clearly seen in the polar radiation patterns of the horn-lens combination which are shown in Figure 4-26. The smooth lens (blue curve) has a large co-polar back-lobe to the left in Figure 4-26(a) but this lobe is dramatically reduced when the grooves are introduced (red curve). For the cross-pol in Figure 4-26(b), the grooves also reduce the back-radiation but the peak in the front hemisphere is increased by 10.6 dB.

To ensure the highest possible accuracy of the simulations, the grooved lens model described here should be included in the GRASP computations of the front end performances. However, due to limitations in computer memory, this model can only be used in Band 3.

Table 4.3 Comparison of various parameters for the smooth and grooved lenses.

	Patches	Unknowns	Reflection	Peak co-pol	Peak cross-pol
Smooth	348	24320	0.32 dB	28.27 dB	-13.6 dB
Grooved	2800	56320	0.03 dB	28.45 dB	-3.0 dB

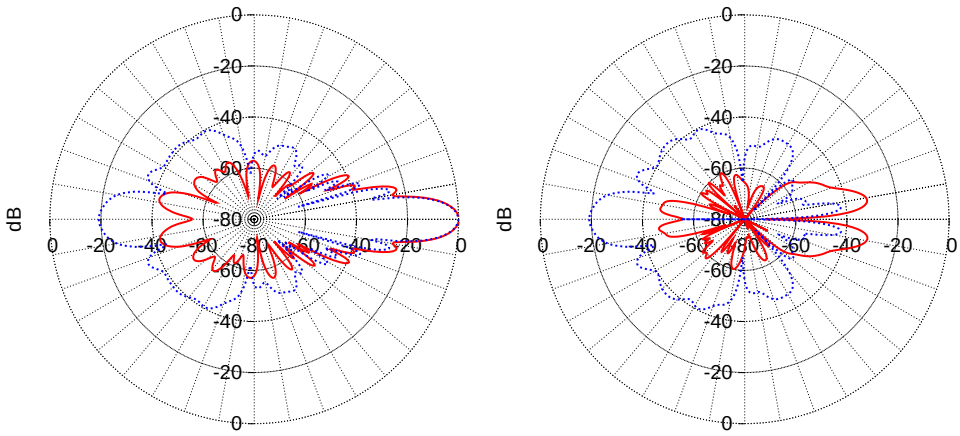

(a) (b)

Figure 4-26 Radiation patterns of the lens with grooves (red curve) and without grooves (blue curve). The E-plane co-polar component is shown in (a) and the cross-polar in (b).

4.3.8 Band 3 summary

- The corrugated horn does not work well at the upper end of the frequency band.
- Lens surface differs from handbook design, but measurements shows that the performance is ok.
- Minor discrepancies between the location and tilt angle of mirror 2 between the specifications in [1] and the drawings in [4].
- The lens grooves can be accurately analysed by the Method of Moments in GRASP which shows that the gooves improve the peak gain by 0.18 dB and increase the cross-polar by approximately 10 dB.

4.4 Band 4

Band 4 is very similar to Band 3, except that there is no lens in the horn aperture. As in Band 3 the system consists of a corrugated horn and two mirrors, where the first mirror (seen from the feed) is ellipsoidal and the second is planar.

A schematic drawing is shown in Figure 4-27 and a 3D-drwaing in Figure 4-28. The mirrors in 4-27 are just symbolic, whereas the mirror diameters in Figure 4-28 correspond to $5w$.

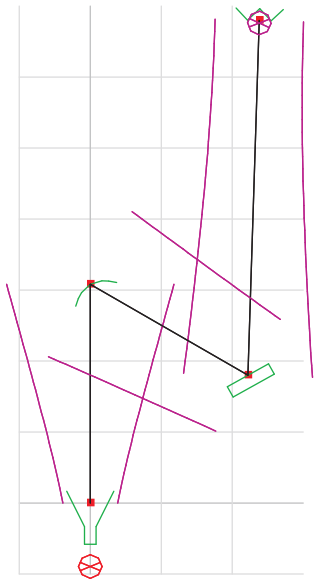

Figure 4-27 Schematic drawing of Band 4. A beam of width $5w$ is shown, corresponding to $-54.3dB$. Grid spacing $= 50mm$

4.4.1 Feed geometry

The feed is defined in the drawing shown in Figure 4-29 which can be compared to the following values from Tabel 11 in [1], p. 37.

Axial length:	100.04 mm
Aperture diameter:	$D = 24.00$ mm

The aperture diameter agrees with the drawing and the axial length looks correct although it is not directly indicated on the drawing. In Tabel 11 in [1], p. 37 a Gaussian beam model of the feed is used with the input parameters:

Beam radius:	$w = (D/2) \cdot 0.6435$ mm $= 7.722$ mm
Radius of curvature:	$R = 100.04$ mm

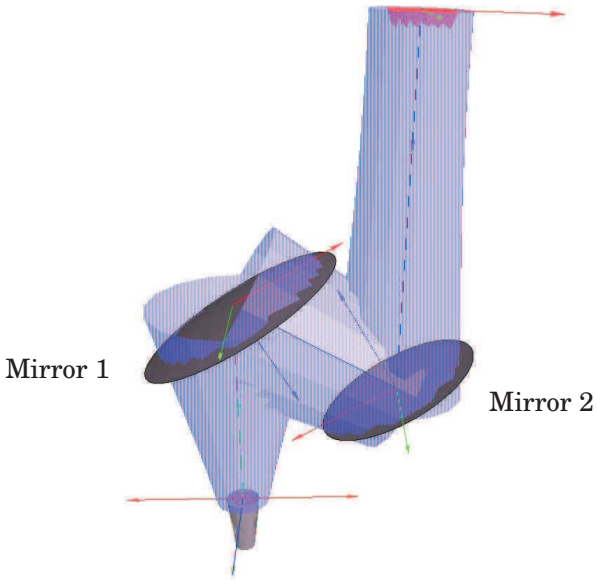

Figure 4-28 3D drawing of Band 4 at 144 GHz. A beam of radius $5w$ is shown, corresponding to $-54.3dB$.

The other data in the table have been compared to the drawings in [5] and they agree except for the distance $d2 = 128.268$ mm which is 131.392 mm on the drawing in [5], p. 41. We assume that the value on the drawing is correct, and it also gives the best agreement with the derived beam data in the table.

In the following GRASP analysis a hybrid-mode feed model is used which is a good approximation to the actual corrugated horn with the given aperture diameter and axial length.

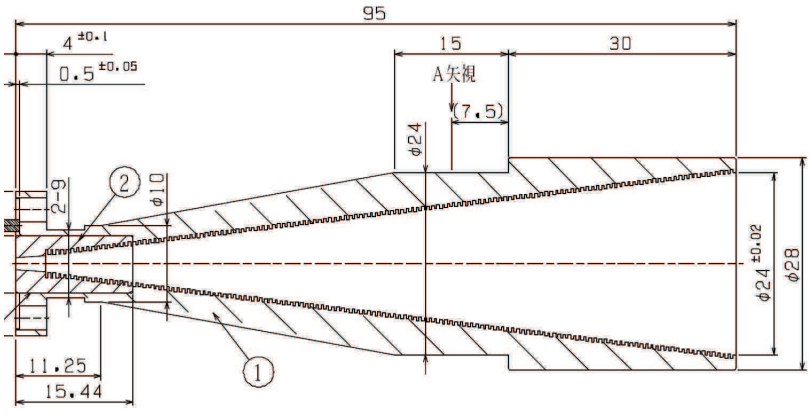

Figure 4-29 Band 4 horn geometry, from [5], p.36

4.4.2 Mirror 1 geometry

Mirror 1 is an ellipsoid defined by the drawings in Figure 4-30.

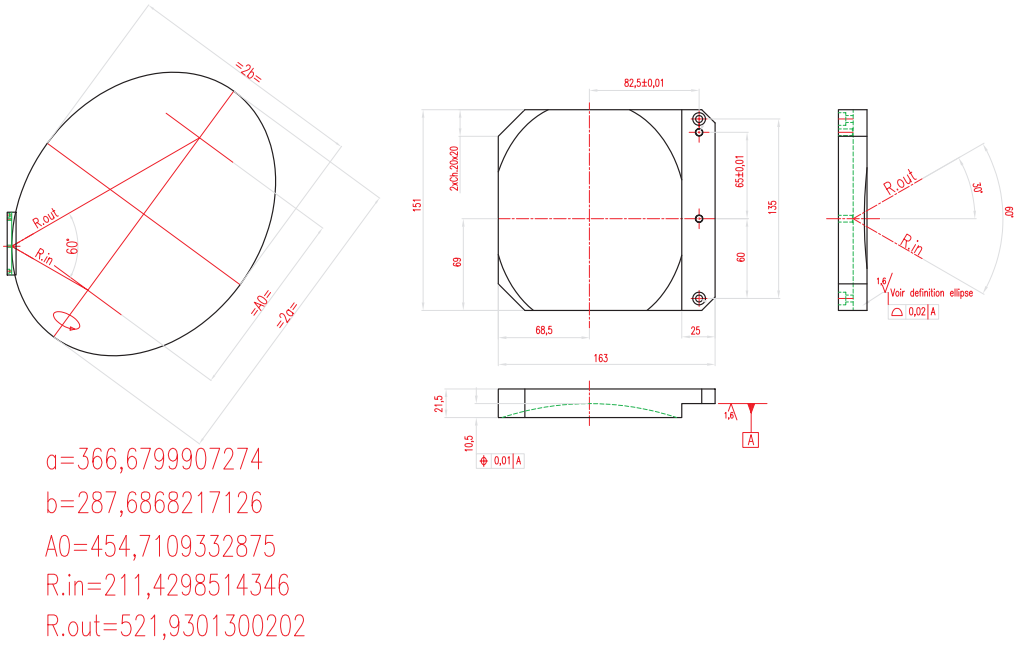

Figure 4-30 Mirror 1 drawing. From [5], p. 44.

If the definition data of the ellipsoid is chosen as the half axes a and b from Figure 4-30 and the angle of incidence $\theta_{in} = 30°$ it is possible to derive the other ellipsoid parameters. The focal length becomes $f = 150.4740$ mm in agreement with Table 11 in [1], p. 34. The rim is also defined in Figure 4-30 where it is indicated that the plane of the rim is parallel to the surface tangent plane in the centre reflection point, and that the distance from this point to the rim plane is 10.500 mm. From this definition the rim curve becomes a planar ellipse, but with cut-offs as defined on the drawing. It has been checked that these data are consistent and that they agree with the other data on the drawing.

4.4.3 Mirror 2 geometry

Mirror 2 is planar with dimensions shown in Figure 4-31 and according to [5], p. 45 it is located in the distance 131.392 mm from mirror 1. This value is used in the following calculations instead of the different value 128.268 mm given in Table 11 in [1], p. 34. The tilt angle of mirror 2 results in a beam tilt of $1.8929°$ according to [5], p. 41,which is different from the tilt angle $1.92°$ in [1], p. 18. (redefined 2007-04-10).

4.4.4 Cryostat window and filter geometry

According to [5], p. 41, the cryostat window is located 49.500 mm above the feed aperture. The information in [11] (as summarized below in Table 4.4) then defines the positions and diameters of the window and filters.

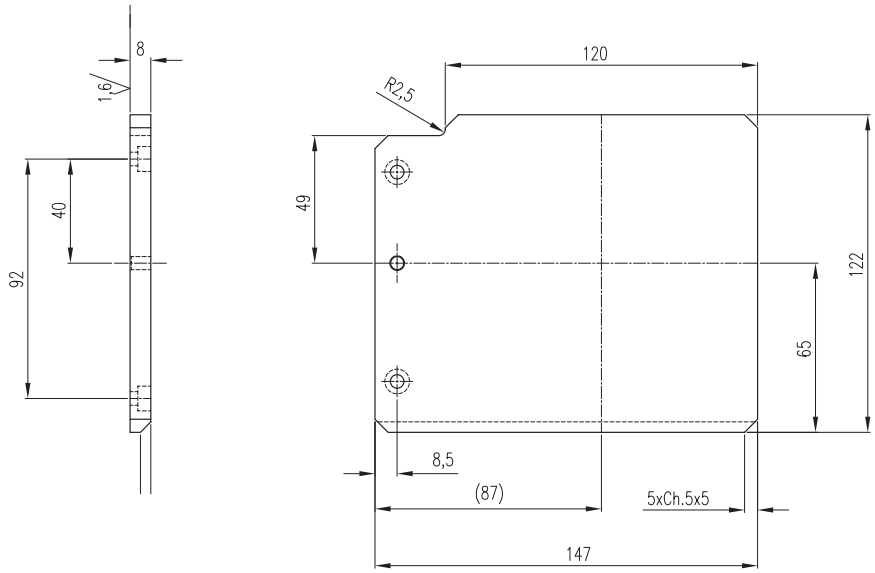

Figure 4-31 Mirror 2 drawing. From [5], p. 45.

	Cryostat window	110K filter	15K filter
z-coordinate	0	27	38
diameter	66	58	40

Table 4.4 Band 4 cryostat window and filters. z-coordinate and diameter (in mm).

The complete set-up of mirrors and windows is shown in Figure 4-32.

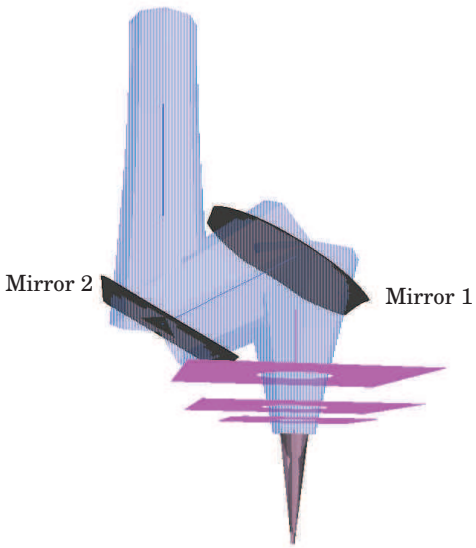

Figure 4-32 Band 4 geometry with mirrors, filters and cryostat window

4.4.5 GRASP analysis results

GRASP analysis of the front end system is presented below. In Figure 4-33 the far field from the mirror system is computed without taking into account the filter and window apertures and the results are compared to an ideal Gaussian beam. For the Band 4 front-end system the ideal output beam has a waist radius of $w_0 = 12.4534$ mm at 144 GHz.

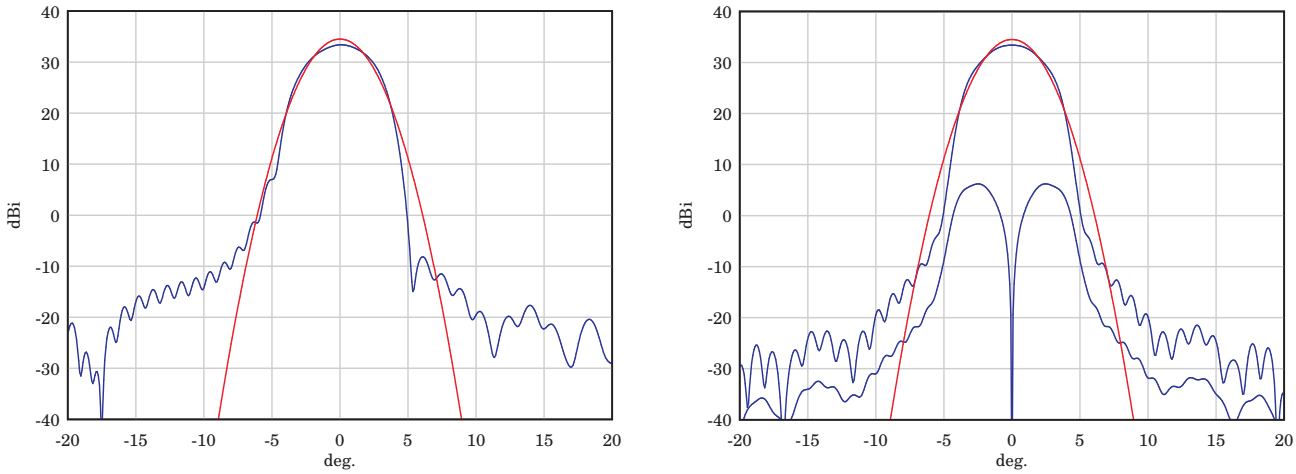

Figure 4-33 Far-field beams for mirror system with hybrid mode feed (blue curves) and ideal Gaussian output beam (red curves). Polarisation along x, i.e. in the plane of symmetry.
Left figure: $\phi = 0°$. Right figure: $\phi = 90°$.
Frequency: 144 GHz

It is seen that there is a significant loss in peak gain which is due to a different beam shape and due to power in the sidelobes. The power loss due to truncation is low and shown below in Table 4.5.

	Relative incident power
15K filter	0.9993
110K filter	0.9993
Cryostat Window	0.9988
Mirror 1	0.9985
Mirror 2	0.9984

Table 4.5 Power loss through apertures and mirrors. Dielectric reflection loss is not included for the apertures.

Far-field cuts with and without filter and cryostat apertures are shown in Figure 4-34. The effect of the apertures (without dielectrics) is only significant at levels -40 dB below peak.

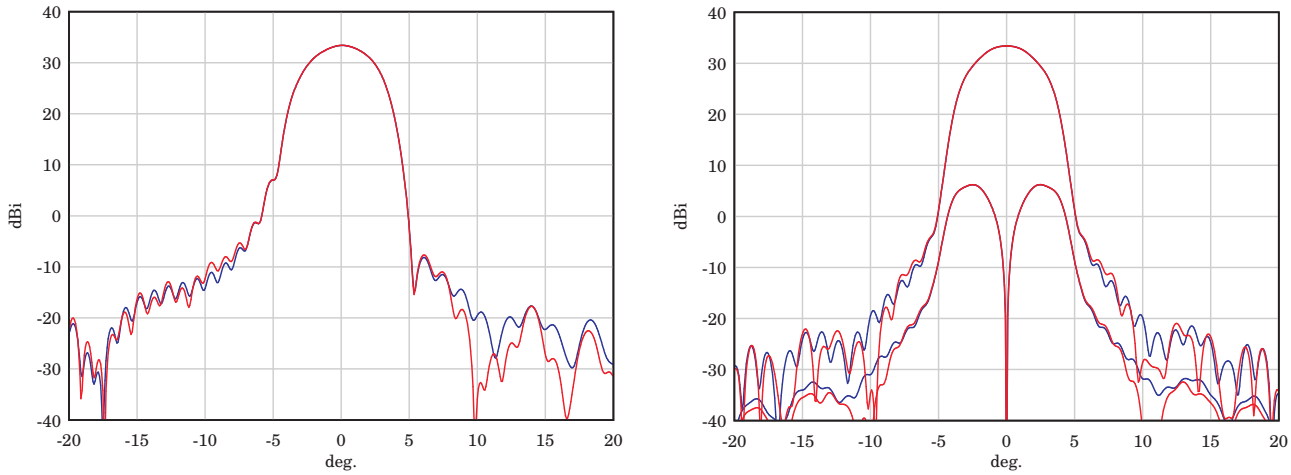

Figure 4-34 Far-field beams for mirror system without apertures (blue curves) and with apertures (red curves). Polarisation along x, i.e. in the plane of symmetry.
Left figure: $\phi = 0°$. Right figure: $\phi = 90°$.
Frequency: 100 GHz

4.4.6 Band 4 summary

- Minor discrepancies in the location and tilt angle of mirror 2 between the specifications in [1] and the drawings in [5].

4.5 Band 5

The Band 5 sub-system consists of a corrugated horn and two ellisoidal mirrors. A schematic drawing is shown in Figure 4-35 and a 3D-drwaing in Figure 4-36. The reflector diameters correspond to $5w$. It is seen that the Gaussian beam has a waist located between the two mirrors.

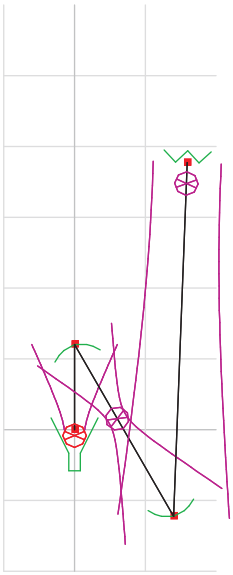

Figure 4-35 Schematic drawing of Band 5. A beam of width $5w$ is shown, corresponding to $-54.3dB$. Grid spacing $= 50mm$

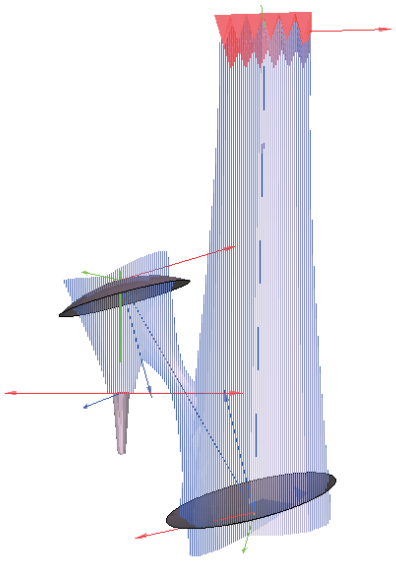

Figure 4-36 3D drawing of Band 5 at 187 GHz. A beam of radius $5w$ is shown, corresponding to $-54.3dB$.

A detailed analysis would need the feed pattern and the shape and position of the reflector rim curves and information about the

IR-filters and cryostat windows.

As an experiment, until the correct data become available, a simple model of the cryostat window is constructed as shown in Figure 4-37. The window is circular with diamater $d = 60mm$ and loacted in an infinite conducting screen through the output waist. It is assumed that the dielectric constant of the window material is $\varepsilon_r = 2.1$ and thickness $h = 2.77mm$. The thickness is equal to $5\lambda_m/2$, where $\lambda_m = 1.106mm$ is the wavelength at $187GHz$ in the dielectric material. This statisfies the condition for minimum reflection, which states that the thickness must be an integer multiple of $\lambda_m/2$.

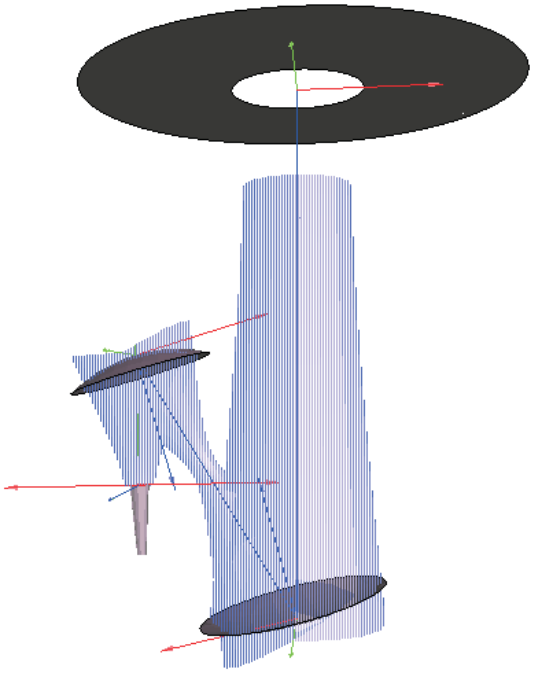

Figure 4-37 3D drawing of Band 5 with cryostat window

The far-field radiation with and without the cryostat window is shown in Figure 4-38. It is seen that the window has very little effect on the beam shape, but the diffraction effects are reduced. A closer examination of the data shows that the window reduces the peak directivity by app. $0.01dB$, whereas a non-ideal thickness such as $4.5\lambda_m/2$ reduces the directivity by $0.6dB$.

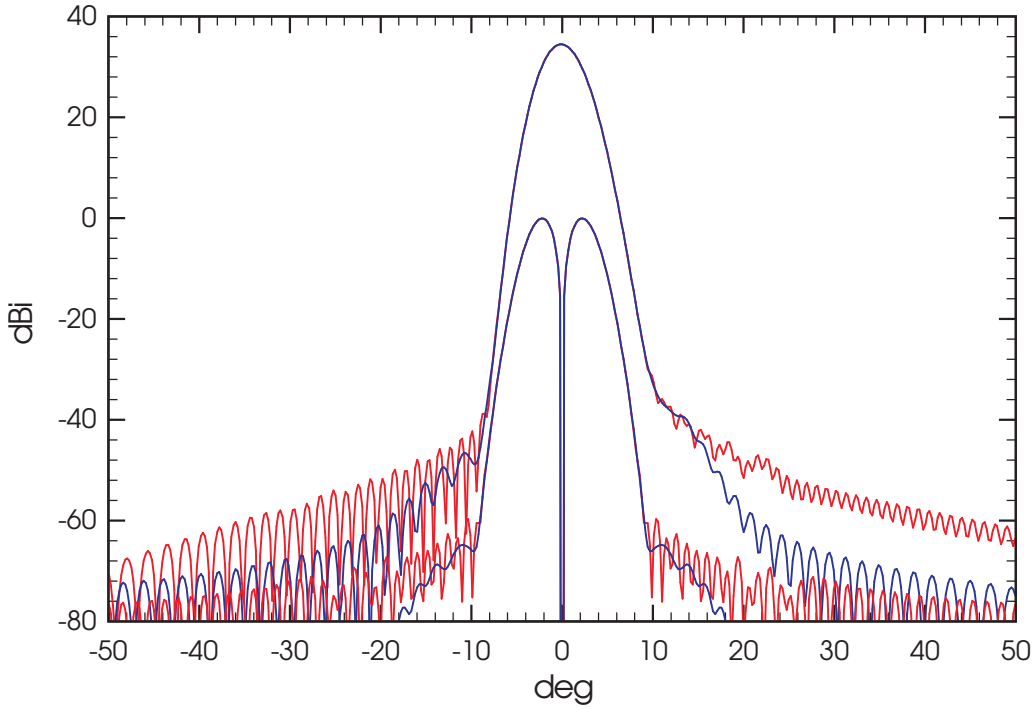

Figure 4-38 Far-field radiation of Band 5 with and without cryostat window.
Co-pol. $\phi = 0°$ and cx-pol. $\phi = 90°$.
Red curve: without cryostat window.
Blue curve: with cryostat window.

4.6 Band 6

The band 6 sub-system is very similar to band 5 and consists of a corrugated horn and two ellipsoidal mirrors. A schematic drawing is shown in Figure 4-39 and a 3D-drwaing in Figure 4-40. The mirrors in Figure 4-39 are just symbolic, but the mirror diameters in Figure 4-40 correspond to $5w$. It is seen that the Gaussian beam has a waist located between the two mirrors.

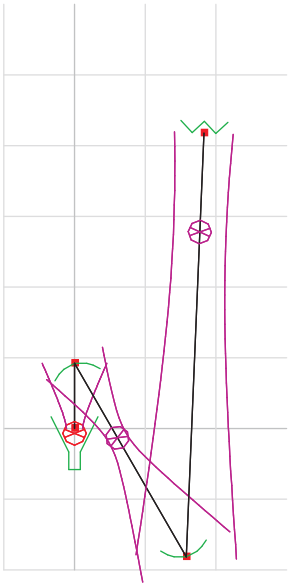

Figure 4-39 Schematic drawing of band 6. A beam of width $5w$ is shown, corresponding to $-54.3dB$. Grid spacing $= 50mm$

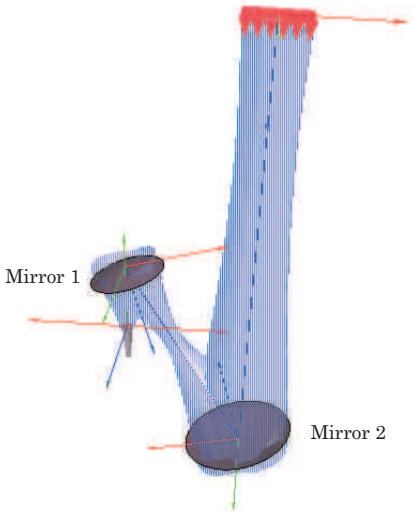

Figure 4-40 3D drawing of band 6 at 243 GHz. A beam of radius $5w$ is shown, corresponding to $-54.3dB$.

The front-end model in GRASP for band 6 is described in the

following subsections. The required data is found in the reports [1] and [6].

4.6.1 Feed geometry

The feed is defined by the drawing shown in Figure 4-41.

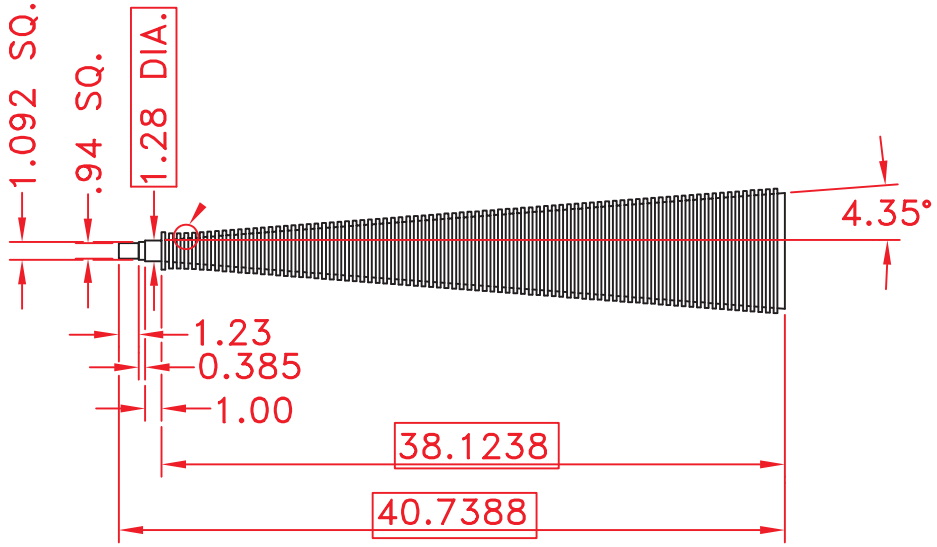

Figure 4-41 Band 6 feed geometry, from [6], p.54

From this it is computed:

Aperture diameter:	$D = (38.1238 \cdot \tan 4.35°) \cdot 2 + 1.28 = 7.0800$ mm
Axial length:	$38.1238 + 1.28/(2 \cdot \tan 4.35°) = 46.5375$ mm
Slant Length:	Axial length$/\cos 4.35° = 46.6718$ mm

These numbers are in agreement with Tabel 13, p.38 in [1]. The radiation from the horn can be approximated by a Gaussian beam with the following parameters at the horn aperture:

Beam radius:	$w = (D/2) \cdot 0.6435 = 2.2780$ mm
Radius of curvature:	$R = 46.6718$ mm

In order to have agreement with the Gaussian beam parameters given in Table 13, p.38 [1] it is necessary to use the number 0.6435 (see [12]) for the ratio between beam radius and aperture radius. It is also necessary to use the slant length of the horn as the radius of curvature and not the axial length. Perfect agreement with the beam parameters in Table 13 is then obtained.

The aperture diameter calculated above and the given flare angle is used as input for the hybrid mode feed model in Grasp.

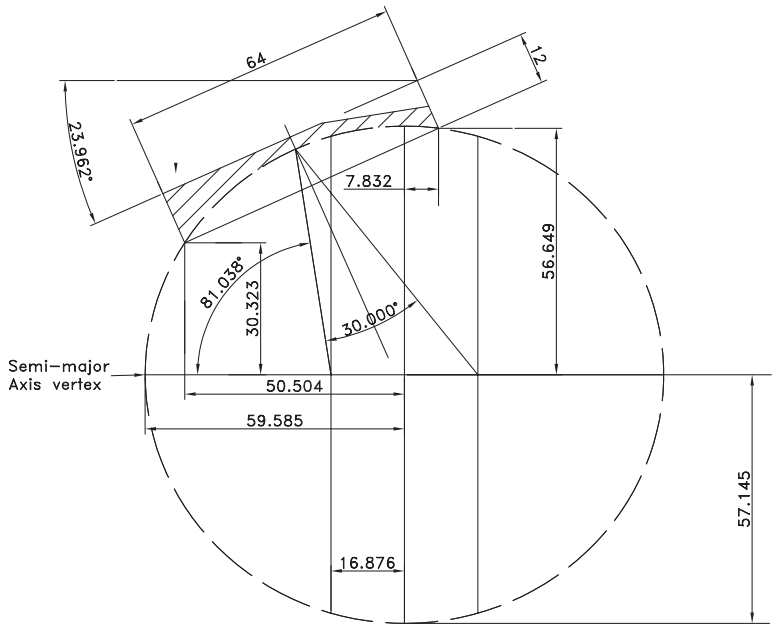

Figure 4-42 Band 6 Mirror 1 geometry, from [6], p.54

4.6.2 Mirror 1 geometry

Mirror 1 is defined by the drawing in Figure 4-42.

The data on the figure overspecify the ellipsoidal surface so we have chosen to use the following as input and derive all other quantities needed for the Grasp analysis:

Half major axis:	$a = 59.5850$ mm
Half minor axis:	$b = 57.1450$ mm
Offset angle:	$\phi = 81.0380°$

From this it is calculated:

Half foci distance:	$c = \sqrt{a^2 - b^2} = 16.8766$ mm
Eccentricity:	$e = c/a = 0.2832$
Input focal distance:	$r_{in} = b^2/(a \cdot (1 + e\cos\phi)) = 52.4890$ mm
Output focal distance:	$r_{out} = 2a - r_{in} = 66.6810$ mm
Focal length:	$f = 1/(1/r_{in} + 1/r_{out}) = 29.3700$ mm
Angle of incidence:	$\theta_{in} = \arccos((r_{in}^2 + r_{out}^2 - (2c)^2)/(2r_{in}r_{out}))/2$ $= 15.0004°$

Next, the rim of the mirror is determined. The rim is a planar ellipse of which the coordinates of the major axis is given in Figure 4-42. As input we use only the z-coordinates and derive the other data.

z-coordinates of rim:	$z_1 = -50.5040$ mm
	$z_2 = 7.8320$ mm

The equation $z^2/a^2 + (x^2+y^2)/b^2 = 1$ of the ellipsoid then gives:

x-coordinates of rim:	$x_1 = 30.3236$ mm
	$x_2 = 56.6492$ mm
Distances to rim	$\ell_1 = 45.2804$ mm
	$\ell_2 = 61.8033$ mm
Half major axis of rim:	$a_{el} = \frac{1}{2}\lvert P_1P_2\rvert = 32.0005$ mm
Half minor axis of rim:	$b_{el} = \frac{1}{2}\sqrt{(2a_{el})^2 - (\ell_1 - \ell_2)^2} = 30.9157$ mm
Tilt angle of surface normal with respect to rim normal:	
	$\alpha = \arctan((x_2 - x_1)/(z_2 - z_1)) + \phi - \theta_{in} - 90^\circ$
	$= 0.3262^\circ$

where ℓ_1 and ℓ_2 are shown in the following figure.

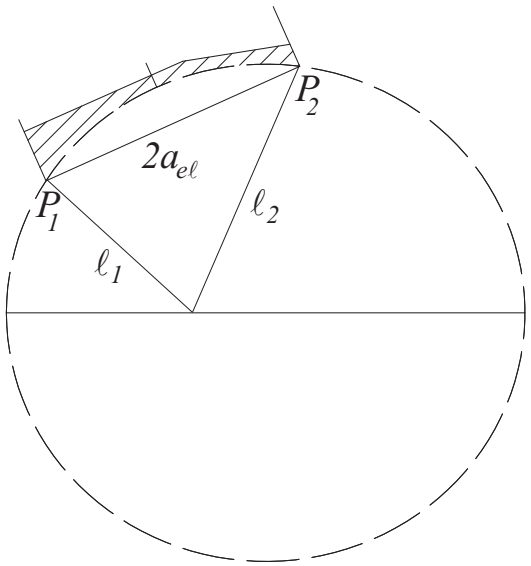

Figure 4-43 Band 6 Mirror 1 rim geometry

The calculations show that the derived data are consistent with the data on the figure, but it is noted that the tangent plane of the surface in the centre point deviates 0.3262° from the plane of the rim.

4.6.3 Mirror 2 geometry

Mirror 2 is defined by the drawing in Figure 4-44.

The data on the figure overspecify the ellipsoidal surface, so the following data is chosen as input from which the other ellipsoidal parameters are derived.

Input data:

Half minor axis:	$a = 171.8160$ mm
Half foci distance:	$c = 118.8490$ mm
Offset angle:	$\phi = 45.5460^\circ$

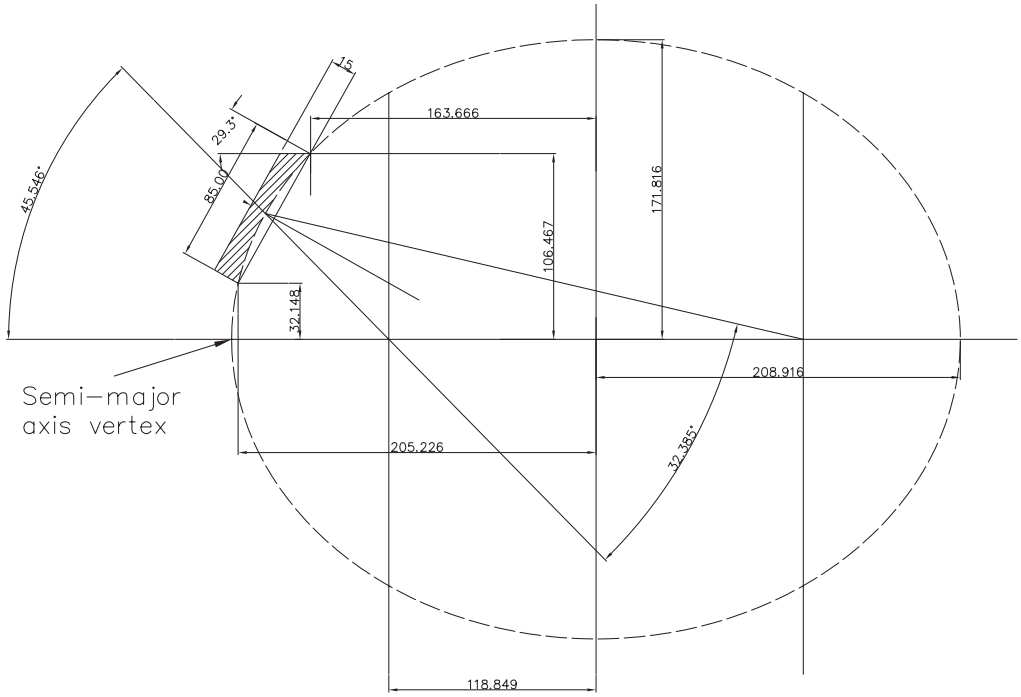

Figure 4-44 Band 6 Mirror 2 geometry, from [6], p.56, updated 2007-03-16

From this it is calculated:

Half major axis:	$a = \sqrt{b^2 + c^2} = 208.9158$ mm
Eccentricity:	$e = c/a = 0.5689$
Input focal distance:	$r_{in} = b^2/(a \cdot (1 + e\cos\phi)) = 101.0465$ mm
Output focal distance:	$r_{out} = 2a - r_{in} = 316.7852$ mm
Focal length:	$f = 1/(1/r_{in} + 1/r_{out}) = 76.6099$ mm
Angle of incidence:	$\theta_{in} = \arccos((r_{in}^2 + r_{out}^2 - (2c)^2)/(2r_{in}r_{out}))/2$ $= 16.1925°$

Next, the rim of the mirror is determined. The rim is a planar ellipse of which the coordinates of the major axis is given in Figure 4-44. As input only the z-coordinates are used.

z-coordinates of rim:	$z_1 = -205.2260$ mm
	$z_2 = -163.6660$ mm

The equation $z^2/a^2 + (x^2 + y^2)/b^2 = 1$ of the ellipsoid then gives:

x-coordinates of rim:	$x_1 = 32.1492$ mm
	$x_2 = 106.7853$ mm
Distances to rim	$\ell_1 = 92.1659$ mm
	$\ell_2 = 115.8088$ mm
Half major axis of rim:	$a_{el} = \frac{1}{2}\lvert P_1P_2\rvert = 42.7135$ mm
Half minor axis of rim:	$b_{el} = \frac{1}{2}\sqrt{(2a_{el})^2 - (\ell_1 - \ell_2)^2} = 41.0451$ mm

Tilt angle of surface normal with respect to rim normal:

$$\alpha = \arctan((x_2 - x_1)/(z_2 - z_1)) + \phi - \theta_{in} - 90^\circ$$
$$= 0.2429^\circ$$

where ℓ_1 and ℓ_2 are shown in the following figure.

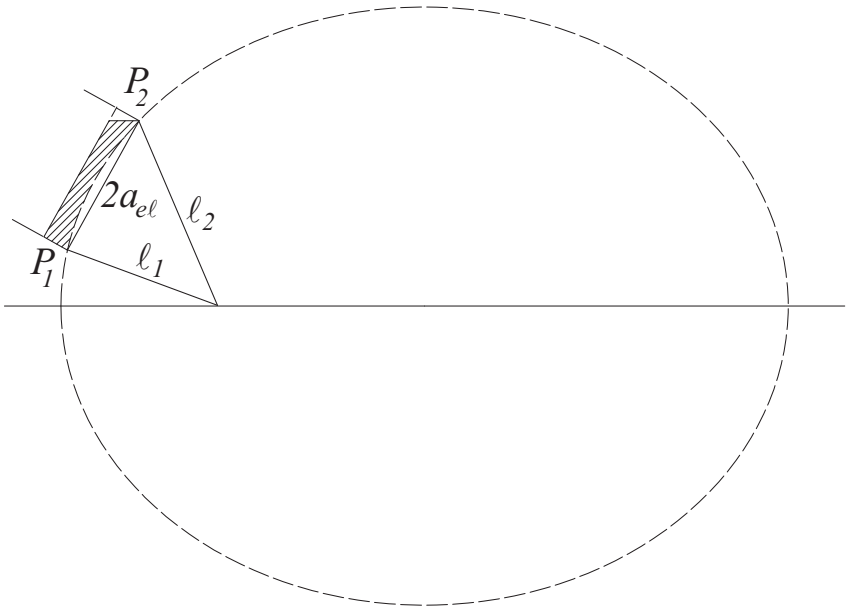

Figure 4-45 Band 6 Mirror 2 rim geometry

It is seen that the derived data deviates a little from the numbers on the drawing, e.g, the coordinates of the upper edge of the rim $(x_2, z_2) = (106.467, 163.666)$ given on the drawing do not fit in the equation of the ellipsoid and the mirror size $2a_{el} = 85.4270$ mm is half a millimetre larger than indicated in the figure. These inconsistencies are, however, so small that they should not have any significant effect on the electrical performance.

The angle of the output beam with respect to the subreflector axis can now be calculated as $2 \cdot 16.1925^\circ - 2 \cdot 15.0004^\circ = 2.3842^\circ$ which is in agreement with table 13, p.38 [1], but not with Table 3, p.18 [1], where this angle is given as 2.34°.

4.6.4 Cryostat window and filter geometry

The position of the cryostat window is determined from Tabel 3, p.18 in [1] where it is specified that it should be located 15 mm above the output beam waist (at 243 GHz). Furthermore, the output waist is located in the distance 229.996 mm from Mirror 2 measured along the beam according to Table 13, p.38 in [1] and in agreement with our calculations. The relative positions and the diameters of the window and filters are then given in [11], as summarized below in Table 4.6.

	Cryostat window	110K filter	15K filter
z-coordinate	0	49	81
diameter	50	61	65

Table 4.6 Band 6 cryostat window and filters. z-coordinate and diameter (in mm).

From these data it is possible to set-up the mirror and window geometry in GRASP as shown in Figure 4-46.

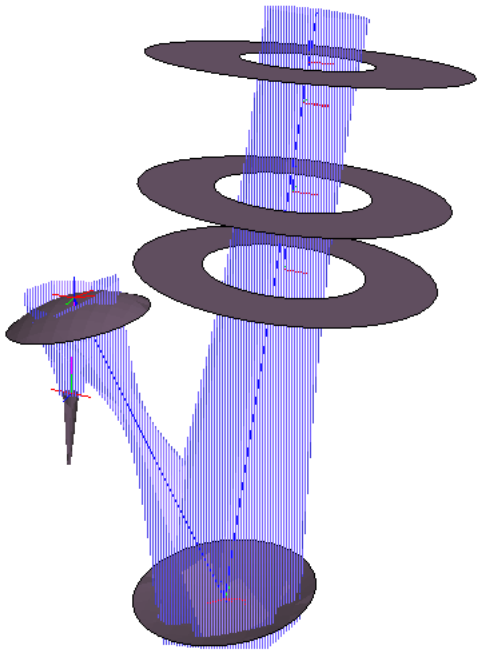

Figure 4-46 Band 6 geometry with mirrors, filters and cryostat window. The mirrors are drawn to their actual size and beam of diameter $5w$ is shown.

4.6.5 GRASP analysis results

GRASP analysis of the mirror system including the filters and cryostat window is presented in this section. In the first results in Figure 4-47 the far field from the mirror system is computed without taking into account the filter and window apertures. The results are compared to the ideal output of the band 6 front-end system, which should be a Gaussian beam with waist $w_0 = 7.4490$ mm.

The next results in Figure 4-48 includes the filters and window, but treated as apertures in infinite conducting screens, with no

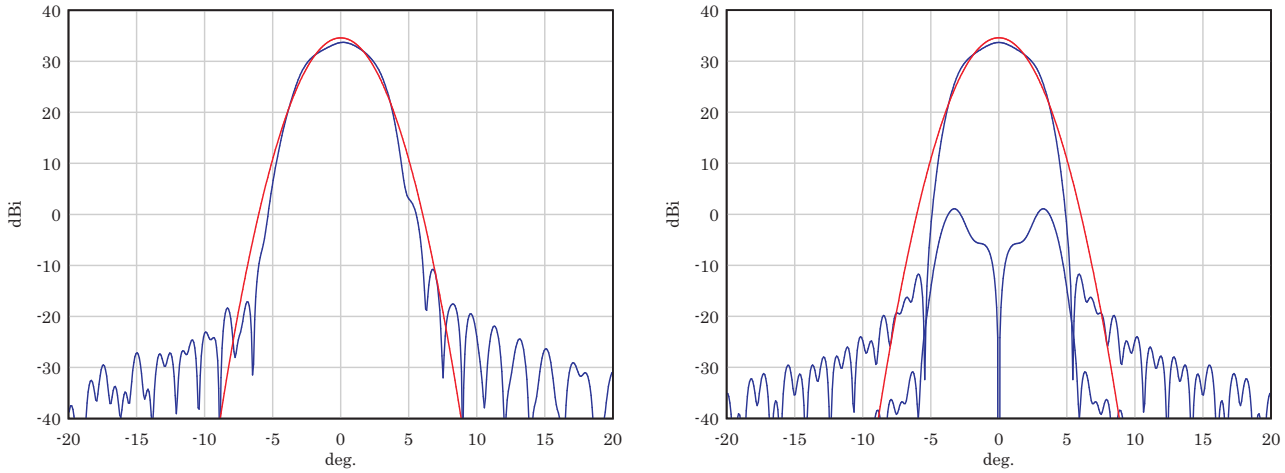

Figure 4-47 Far-field beams for mirror system with hybrid mode feed (blue curves) and ideal Gaussian output beam (red curves). Polarisation along x, i.e. in the plane of symmetry.
Left figure: $\phi = 0°$. Right figure: $\phi = 90°$.
Frequency: 243 GHz

dielectric material inserted in the apertures. It is seen that the effect of the apertures is only significant 40 dB below peak.

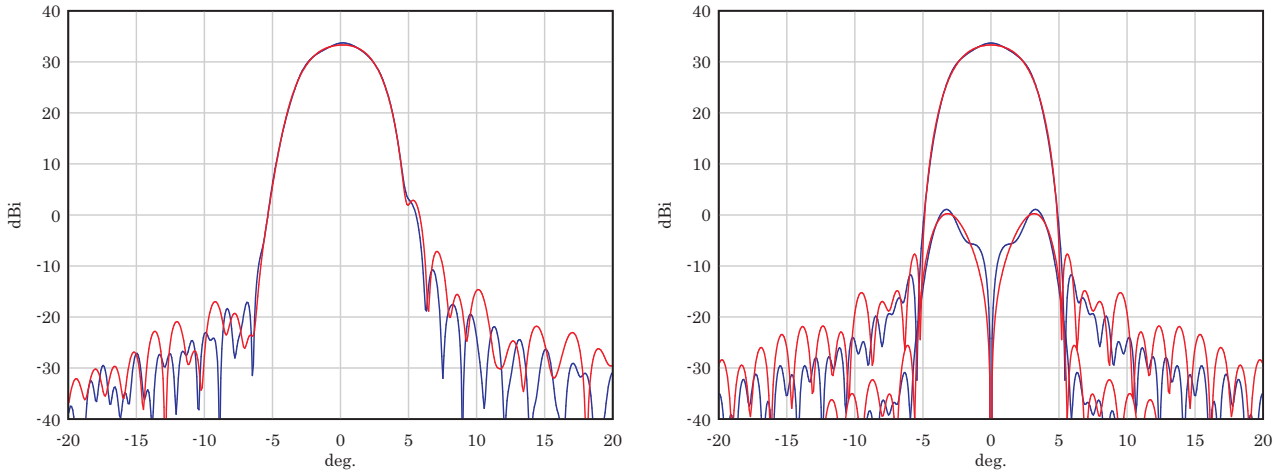

Figure 4-48 Far-field beams for mirror system without apertures (blue curves) and with apertures (red curves). Polarisation along x, i.e. in the plane of symmetry.
Left figure: $\phi = 0°$. Right figure: $\phi = 90°$.
Frequency: 243 GHz

The power loss through the system is illustrated in Table 4.7.

To estimate the importance of multiple interactions between the apertures a calculation with double diffractions between the cryostat window aperture and the 110K-filter aperture is shown in

	Relative incident power
Mirror 1	0.9983
Mirror 2	0.9981
15K filter	0.9979
110K filter	0.9979
Cryostat Window	0.9973

Table 4.7 Power loss through mirrors and apertures. Dielectric losses not included.

Figure 4-49. This means that the field incident of the cryostat aperture is diffracted back to the 115K-filter aperture and then forward again to the cryostat aperture. It is seen that the diffraction effects are very small.

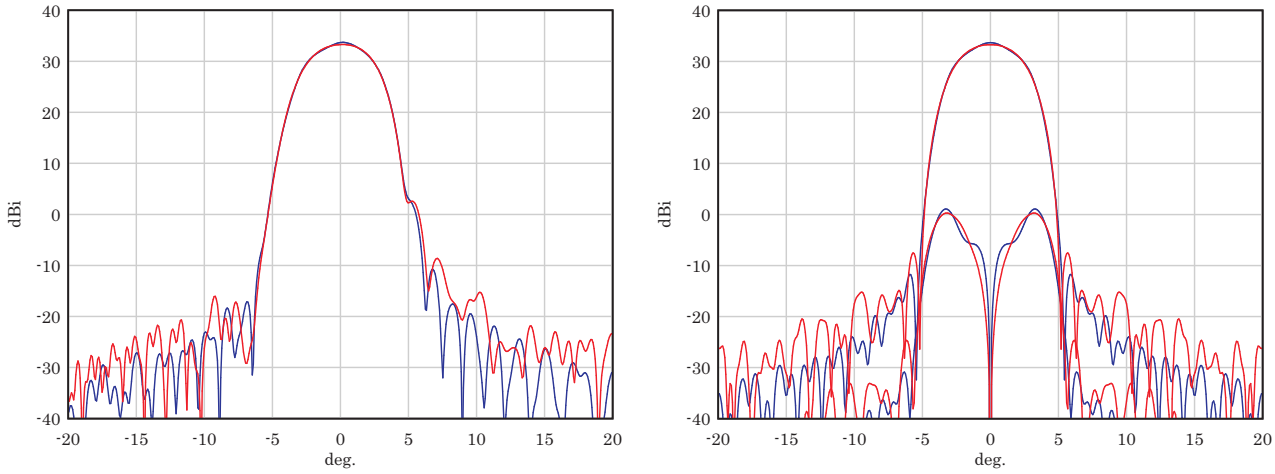

Figure 4-49 Far-field beams for mirror system without apertures (blue curves). Double diffractions included (red curves). Polarisation along x, i.e. in the plane of symmetry.
Left figure: $\phi = 0°$. Right figure: $\phi = 90°$.
Frequency: 243 GHz

In the next calculation the apertures are replaced by dielectric material. This means that the windows are not treated as apertures, but as dielectric disks with diameters equal to those of the apertures. In this way edge diffractions from the apertures are neglected, but transmission loss and double reflections are included. In the present calculation only the cryostat window and the 115K filter is considered. The dielectric material for the cryostat window is quartz with a thickness of 5 mm for which the worst-case reflection loss is measured to app. -17 dB ([1], p.254). This corresponds to a reflection coefficient of 0.14 and a power reflection of 2.0%. In the GRASP model we use this value for the reflection coefficient which is in agreement with the SIS measurements on page 256 of [1], where the absortion loss is 1-2%.

It is not in agreement with the transmission measurements on page 255, where the transmission coefficient is app. -0.4 dB, corresponding to a power transmission of 91%. On page 252 it is, however, mentioned that these measurements are less accurate than the SIS measurements.

In the GRASP model the desired reflection coefficient $R = 0.14$ at 243 GHz is obtained using a dielectric material of thickness 4.83 mm and dielectric constant $\varepsilon_r = 4.2$. This material is also used for the 115K-filter which according to the measurements has a similar reflection coefficient. The results are shown in Figure 4-50 and it is seen that the dielectrics only has small effects.

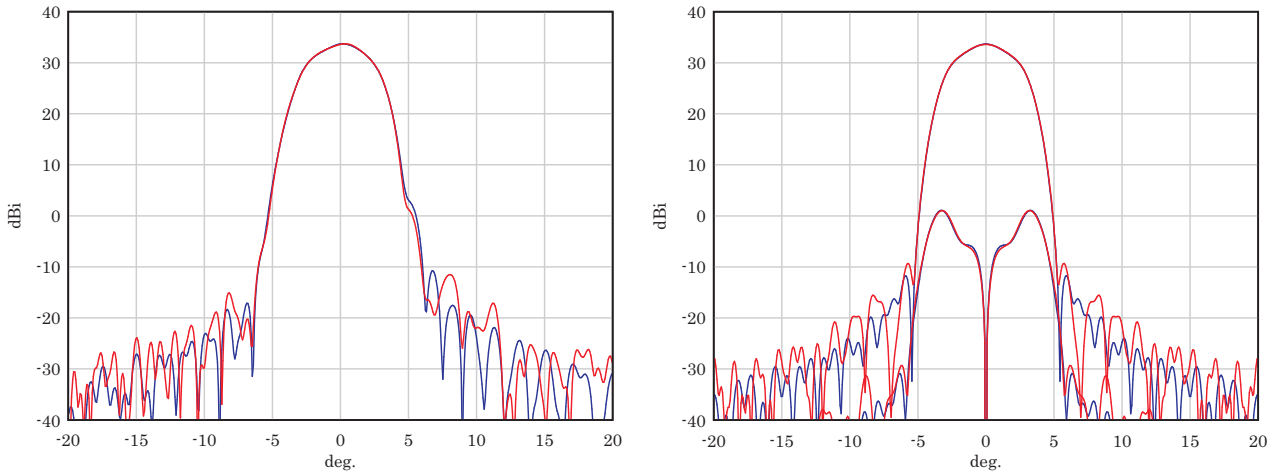

Figure 4-50 Far-field beams for mirror system without apertures (blue curves) and with double reflections included in dielectric windows (red curves). Polarisation along x, i.e. in the plane of symmetry.
Left figure: $\phi = 0°$. Right figure: $\phi = 90°$.
Frequency: 243 GHz

Finally the GRASP calculations with apertures, but without dielectric materials, is compared to a measurement by IRAM [6] p.31. Although we do not know if the orientation of the axes are the same on the two plots it is clear that the isolated side lobes of -33 dB in the measurements cannot be reproduced by the GRASP computations. It is not clear if it is caused by some structures not modelled in GRASP or a problem with the near-field to far-field transformation of the IRAM data.

The units on the axes of the GRASP data is uv which means: $u = \sin\theta\cos\phi$, $v = \sin\theta\sin\phi$.

In [6] it is mentioned that measurements by NRAO have shown that when the system is cooled down in the cryostat a high side lobe appears only 16 dB below the peak (see Figure 42 [6] p.47). The side lobe does not look like a diffraction effect due to e.g. beam

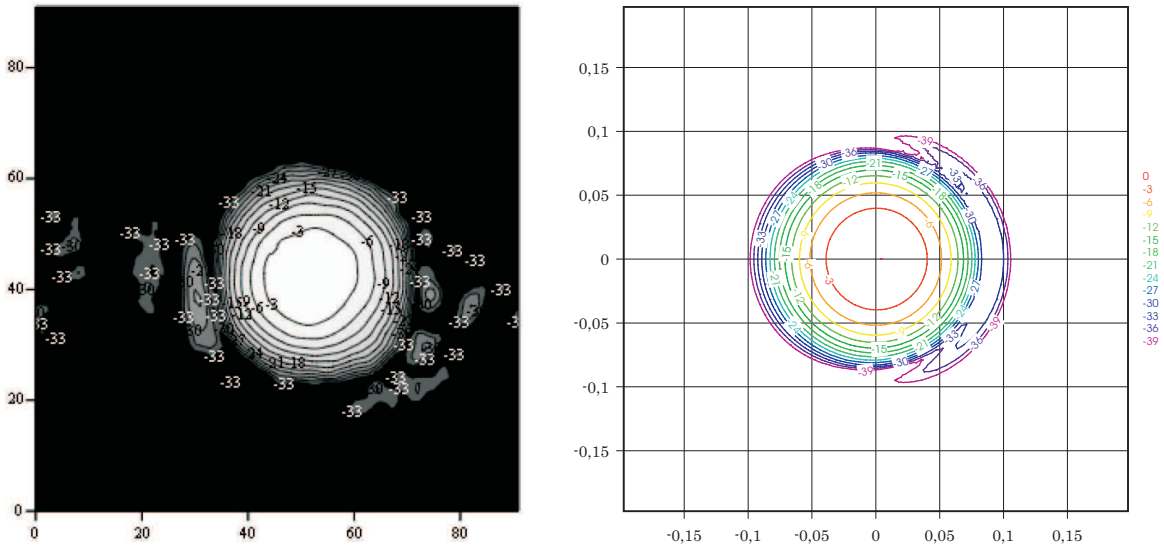

Figure 4-51 Far-field contour plots normalised to 0 dB. Frequency: 246 GHz. Left figure: IRAM data. Right figure: GRASP analysis of mirrors + apertures.

truncation, but could be caused by a change in shape of the mirrors. Since the side lobe only appears on one side of the beam it has some similarity with coma distortion as shown in Figure 4-52. Here a Zernike coma-mode distortion is added to mirror 2 in order to investigate the effect. It is seen that a rather large distortion must be added before a significant side lobe appears and that the level is much lower than -16 dB even for a distortion of 0.3 mm. A further increase of the surface distortion also distorts the main beam such that the side lobe is absorbed and does not appear as a distinct lobe.

At the CDR-meeting at IRAM in May 2007 the solution to the side-lobe problem was presented. It is not related to the temperature of the cryostat, but caused by high reflection in the cryostat window at certain frequencies. The reflected beam is focused at the feed and reflected again in the thick flange of the feed. When the flange of the feed was cut down to a cone-like structure the high side lobe disappeared.

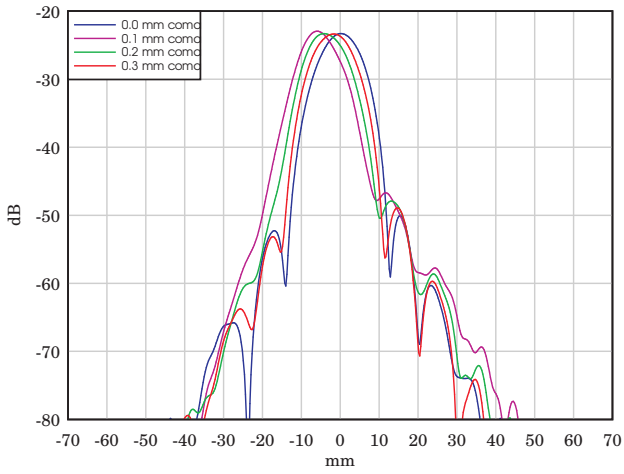

Figure 4-52 Near-field cuts through output waist.
Frequency: 243 GHz.
Coma distortion added to mirror 2.

4.6.6 Band 6 summary

- Minor inconsistencies in the data in [6] for definition of the mirrors.
- Specifications in [1] do not fully agree with the drawings in [6].

4.7 Band 7

The Band 7 sub-system is more complicated than the preceding systems. As in Band 5 and 6 it consists of a corrugated horn and two ellisoidal mirrors, but it also have a polarization beam-splitter located in the beam waist between the two mirrors. A schematic drawing is shown in Figure 4-53. As shown in the 3D-drawaing in Figure 4-54 the beam reflected at the beam splitter is directed towards another ellipsoidal mirror and feed.

The geometry is defined in [7] and some additional geometric information was given to TICRA at the CDR-meeting in Grenoble in May 2007. The two feeds are parallel and also parallel to the directions of the strips in the grid. Seen from a plane orthogonal to the feed directions the two polarisation branches are rotated an angle of 90° corresponding to a rotation of the grid surface of 45°. Otherwise, the two branches are identical with respect to feed geometries and the ellipsoidal surface parameters.

Figure 4-53 Schematic drawing of Band 7. A beam of width $5w$ is shown, corresponding to $-54.3dB$. Grid spacing $= 50mm$

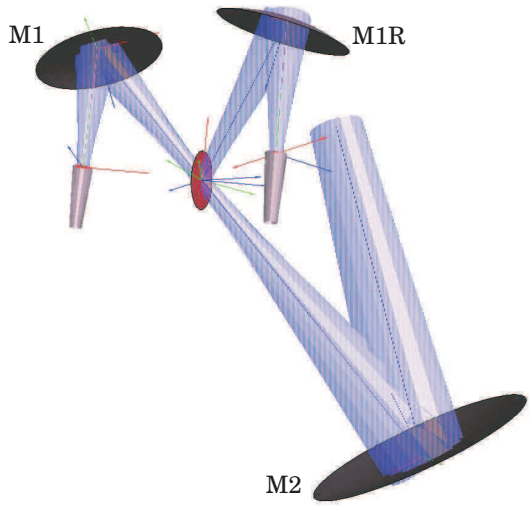

Figure 4-54 3D drawing of Band 7 at 323 GHz. A beam of radius w is shown, corresponding to $-8.69dB$.

4.7.1 Feed geometry

The feed is defined in the drawing shown in Figure 4-55 which can be compared to the following data from Table 14, p. 45 in [1].

Axial length:	45.6832 mm
Aperture diameter:	$D = 6.0045$ mm

The aperture diameter agrees with the drawing and the axial length seems also correct because the flare angles that can be computed from the drawing and the table agree. In Table 14, p. 45 [1] a Gaussian beam model of the feed is used with the following beam parameters:

Beam radius:	$w = (D/2) \cdot 0.6435$ mm $= 1.932$ mm
Radius of curvature:	$R = 45.7817$ mm

The other data in the table have also been compared to the information in [7] and they agree. In the following GRASP analysis a hybrid-mode feed model is used which is a good approximation to the actual corrugated horn with the given aperture diameter and axial length.

4.7.2 Geometry of the mirrors M1 and M1R

The mirrors M1 and M1R are ellipsoidal and defined by the focal distances and angle of incidence given in Table 1, p. 7 in [7]. Both

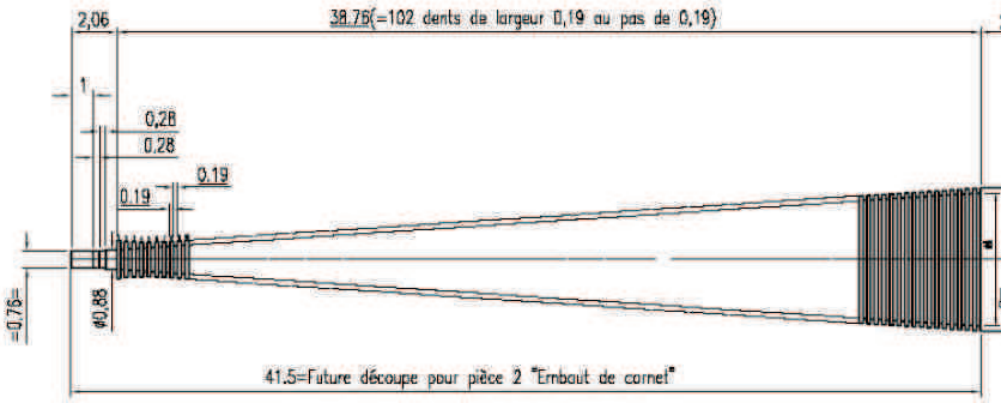

Figure 4-55 Band 7 horn geometry, from [7], p.6

mirrors are located on the same mechanical structure (see Figure 4-56) and the rim shape is found by measuring a number of data points on the drawing. In order to relate the data points to the mirror surfaces it is necessary to know where the centre ray of the beam hits at least one of the surfaces. This information was supplied at the CDR-meeting at IRAM where it was also explained that the distance from the axis of the cartridge to the beam intersection point on M2 is 46.4 mm.

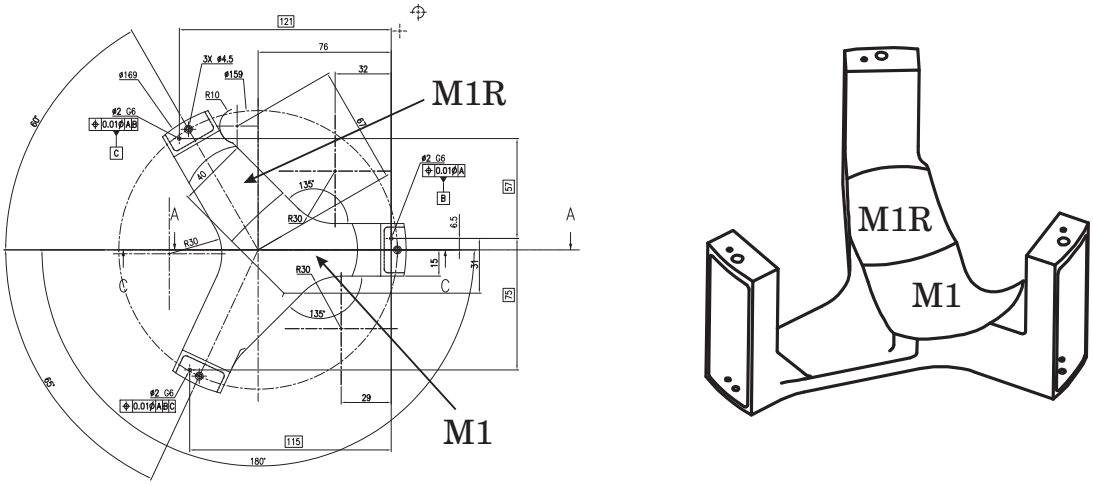

Figure 4-56 Band 7, M1 and M1R geometry.

4.7.3 Geometry of mirror M2

M2 is an ellipsoidal mirror with a surface defined by the data in Table 1, p. 7 in [7]. The tilt angle of the final beam is given as 0.955° which deviates a little from the value 0.97° given in [1], Table 3, p. 20. The rim of M1 is found from the drawing in Figure 4-57 and from the distance 46.4 mm (mentioned above) from the center ray intersection point on M1 to the axis of the cartridge.

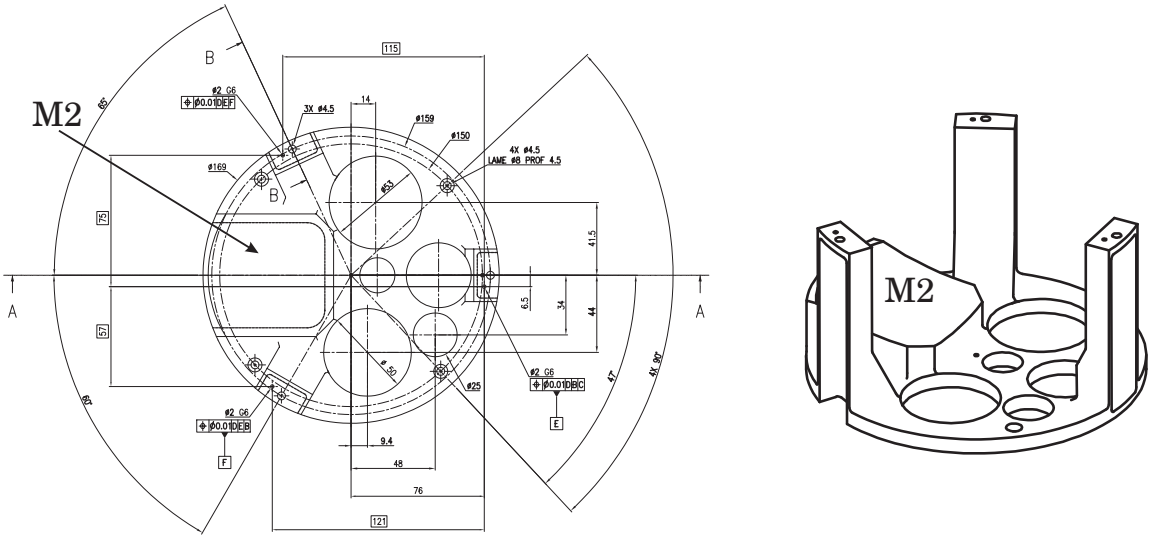

Figure 4-57 Band 7, M2 geometry.

4.7.4 Polarisation grid

A polarisation grid is located on the beam path from M1 to M2 in the distance 63.785 mm from M1. According to a drawing supplied by IRAM the diameter of the grid is 55.85 mm, and it will be assumed that the strip parameters are the same as for band 9, i.e. [8], p. 46,

Grid width:	$10\mu m$
Grid spacing:	$20\mu m$
Grid foil:	Mylar $1.5\mu m$ thick, $\varepsilon_r = 2.8$

A drawing of the grid is shown in Figure 4-58.

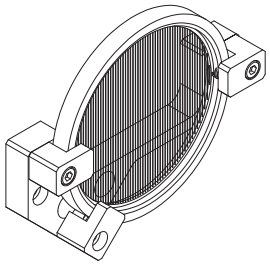

Figure 4-58 Band 7, polarisation grid.

4.7.5 Cryostat window and filter geometry

According to Table 3, p. 20 in [1] the cryostat window is located 67 mm above the nominal output waist position of the front-end system at 323 GHz. The information in Table 2 [1] (as summarized below in Table 4.8 then defines the position and diameters of the

	Cryostat window	110K filter	15K filter
z-coordinate	0	49	81
diameter	40	41	50

Table 4.8 Band 7 cryostat window and filters. z-coordinate and diameter (in mm).

window and filters. In the GRASP analysis the filters and window are treated as apertures without any dielectric material.

The complete set-up of mirrors and windows is showin in Figure 4-59.

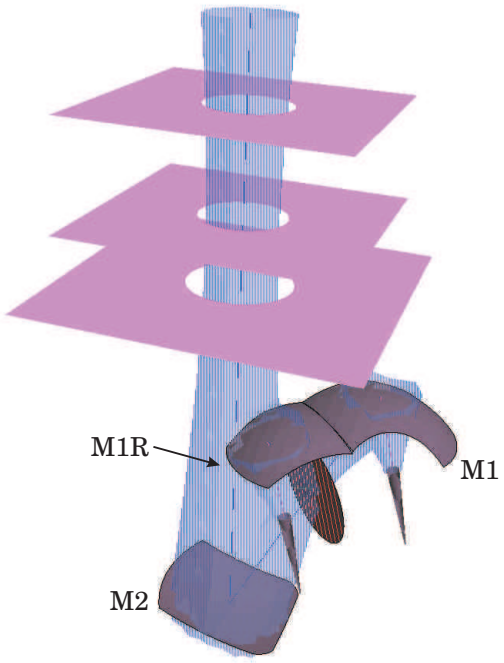

Figure 4-59 Band 7 geometry with mirrors, filters and cryostat window

4.7.6 GRASP analysis results

In Figure 4-60 the far field from the front end is computed without taking into account the filter and window apertures. Beams for the branch transmitted through the grid is compared to the ideal Gaussian beam which has a waist radius of $w_0 = 5.59$ mm at 324 GHz.

As for the other bands there is a loss in peak gain due to a different beam shape and due to sidelobes and power loss through the system, see Table 4.9 below.

It is seen that the major part of the loss, app. 1.5% occurs at M2.

	Relative incident power Transmitted branch	Relative incident power Reflected branch
M1	0.9984	0.9978
Polarisation grid	0.9984	0.9977
M2	0.9830	0.9826
15K filter	0.9829	0.9824
110K filter	0.9826	0.9822
Cryostat Window	0.9821	0.9817

Table 4.9 Power loss through apertures and mirrors. Dielectric reflection loss is not included for the apertures.

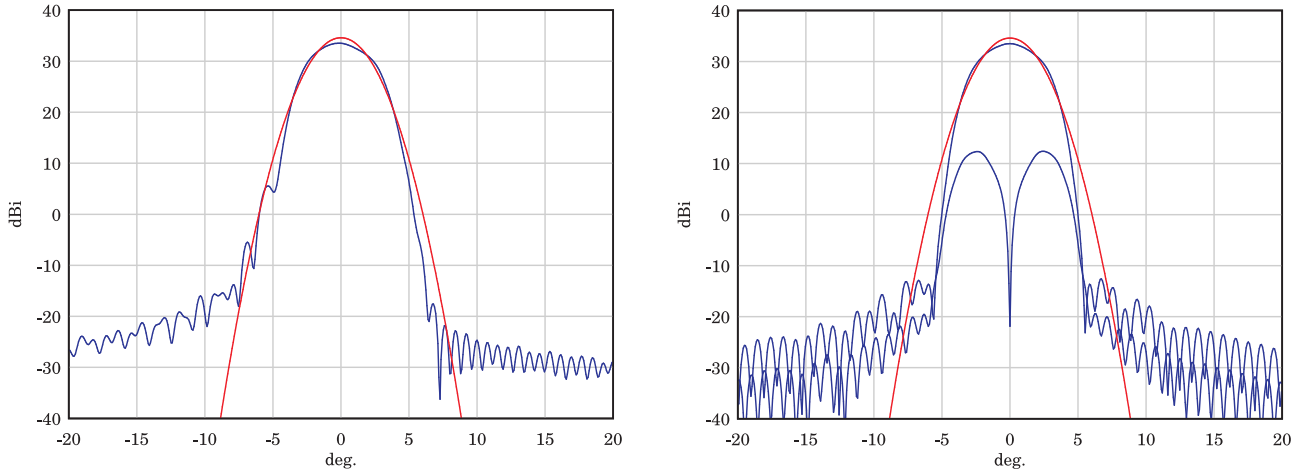

Figure 4-60 Far-field beams for mirror system with hybrid mode feed (blue curves) and ideal Gaussian output beam (red curves). Beam transmitted through the grid.
Left figure: $\phi = 0°$. Right figure: $\phi = 90°$.
Frequency: 324 GHz

Far-field cuts with and without filter and cryostat apertures are shown in Figure 4-61, and a comparison between the branch transmitted through the grid and the branch reflected in the grid is shown in Figure 4-62. It is seen that the apertures and cryostat windows have very little effect and that both branches have high cross polar field at a level app. 21 dB below the copolar peak. In the analysis it is important to use a plane-wave expansion of the incident field on the grid since the grid is located close to a waist, where the field has a significant radial component. A local plane wave assumption is not sufficiently accurate and instead the equivalent currents on the grid must be computed separately for each of the plane waves in the expansion. The front-end system has high cross polar field even though the mirror system is designed such that most of the cross polar generated by M1 will be

compensated by M2. The problem is that the grid removes the cross polar field generated by M1 which should have been used to compensate the cross polar field generated by M2. A preliminary investigation has been carried out to test if a Dragone grid with slightly curved strips could be designed to reduce the cross polar level, but it seems not possible. The reason is that the Gaussian beam modes that represent the cross polar field are $90°$ out of phase with the co-polar mode so that the currents required on the grid for compensation of cross polarisation should have some amount of elliptical polarisation, which is not possible for a grid. A comparison of the system with and without the grid is shown on Figure 4-63 and it is seen that the grid increases the cross polar peak by app. 8.5 dB.

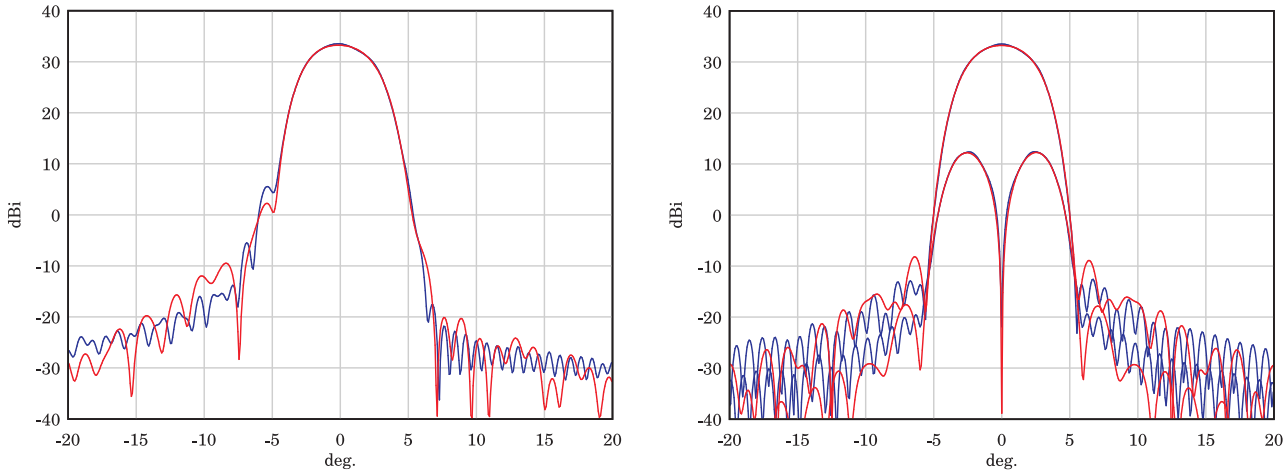

Figure 4-61 Far-field beams for mirror system without apertures (blue curves) and with apertures (red curves). Beam transmitted through the grid. Left figure: $\phi = 0°$. Right figure: $\phi = 90°$. Frequency: 324 GHz

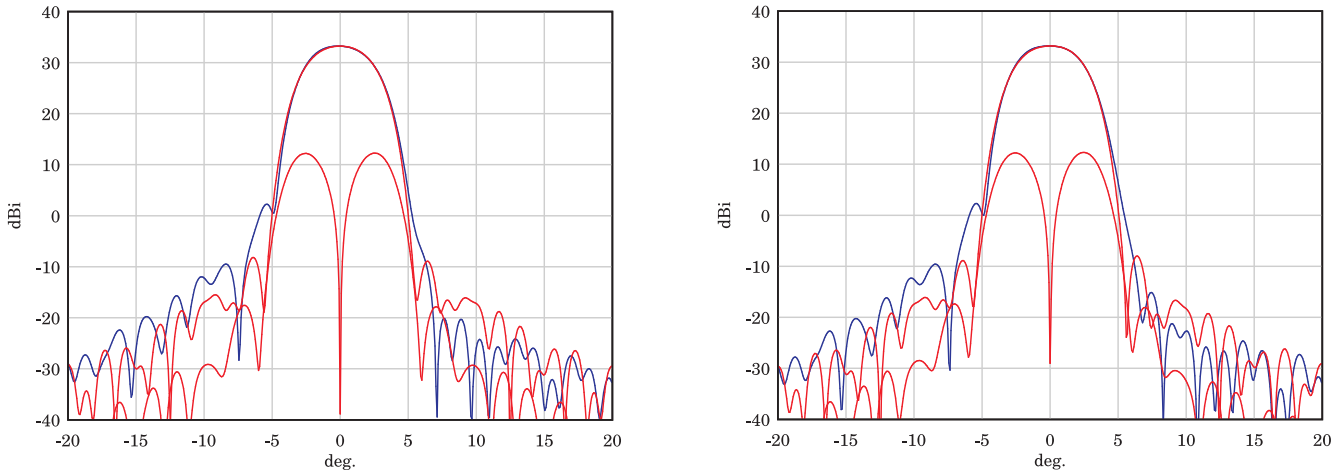

Figure 4-62 Far-field beams for the two polarisation branches, apertures included.
Left figure: Beam transmitted through grid.
Right figure: Beam reflected in grid.
Blue curves: $\phi = 0°$. Red curves: $\phi = 90°$.
Frequency: 324 GHz

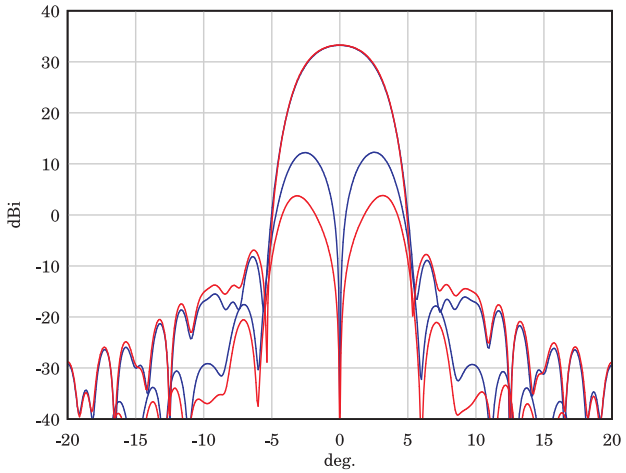

Figure 4-63 Far-field beams for mirror system with grid (blue curves) and without grid (red curves).
$\phi = 90°$ for all curves.
Frequency: 324 GHz

4.7.7 Band 7 summary

- The data in [7] do not fully define the geometry. Additional data was supplied by IRAM.
- The spacing and width of the strips in the polarisation grid are assumed to be identical to the grid in Band 9.
- A loss of power of app. 1.5% occurs at M2.
- High cross polar field due to the polarisation grid.

4.8 Band 8

The Band 8 sub-system has a beam-splitter as in Band 7, but all components are contained in the same plane. After the beam-splitter each branch is reflected in an ellipsoidal mirror. A schematic drawing is shown in Figure 4-64 and a 3D-drwaing in Figure 4-65.

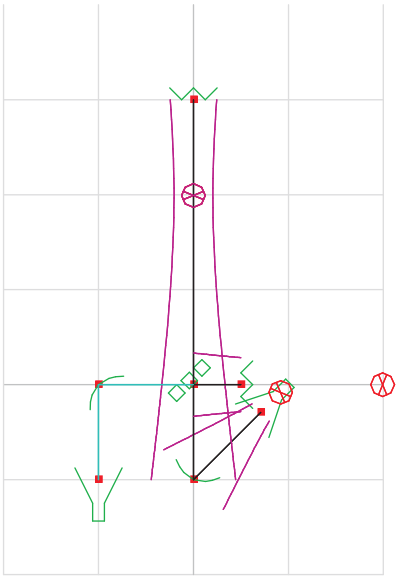

Figure 4-64 Schematic drawing of Band 8. A beam of width $5w$ is shown, corresponding to $-54.3dB$. Grid spacing $= 50mm$

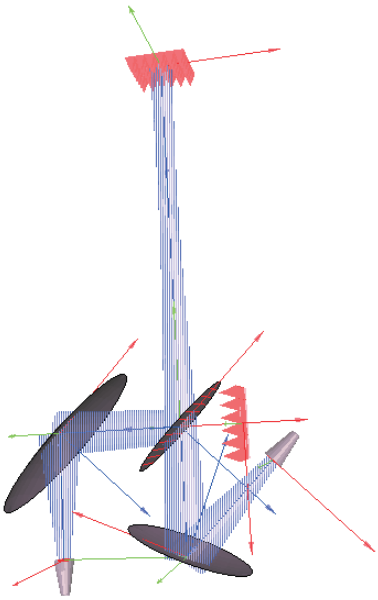

Figure 4-65 3D drawing of Band 8 at 442 GHz. A beam of radius w is shown, corresponding to $-8.69dB$.

A detailed analysis would require feed patterns, the shape and position of the reflector rim curves, polarization grid data and information about IR-filters and cryostat windows. Consequently, the front end will be represented by a simple Gaussian beam model in the GRASP analysis.

4.9 Band 9

The Band 9 sub-system is very similar to Band 7. It consists of a corrugated horn and two ellisoidal mirrors, and it also have a polarization beam-splitter located in the beam waist between the two mirrors. A schematic drawing is shown in Figure 4-66 and a 3D-drawing is shown in Figure 4-67.

The geometry is defined in [8] where it is explained that the two polarization branches are identical, but the reflected branch is rotated 125° around an axis through the centre of the grid. The rotation axis is parallel to the axis of the cartridge and alos parallel to the strips on the grid and to the axes of the two horns. Besides the polarization beam-splitter each branch also has a power beam-splitter through which a local oscillator signal is coupled.

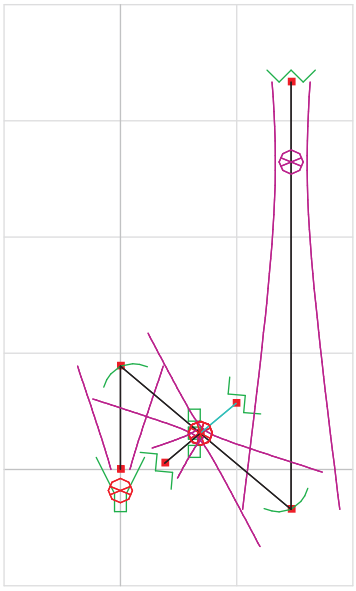

Figure 4-66 Schematic drawing of Band 9. A beam of width $5w$ is shown, corresponding to $-54.3dB$. Grid spacing $= 50mm$

4.9.1 Feed geometry

The feed is defined in the drawing shown in Figure 4-68 which can be compared to the following data from Table 16, p. 51 in [1].

Axial length:	$\ell = 15.52$ mm
Aperture diameter:	$D = 5.07$ mm
Flare angle:	$\arctan(D/(2\ell)) = 9.28^\circ$

In the following calculations a hybrid-mode feed model is used based on the values from the drawing. This is a good approximation to the actual corrugated horn.

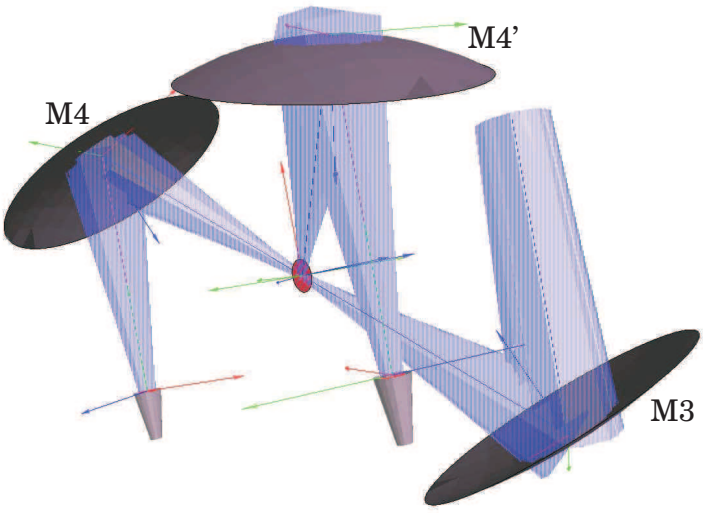

Figure 4-67 3D drawing of Band 9 at 661 GHz. A beam of radius w is shown, corresponding to $-8.69dB$.

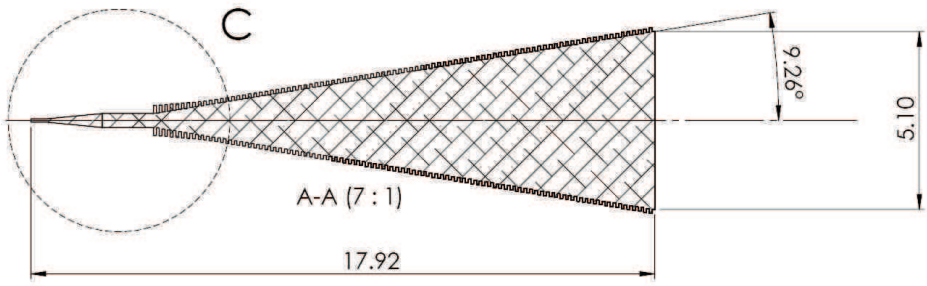

Figure 4-68 Band 9 feed geometry, from [8], p. 62

4.9.2 Geometry of the mirrors M4 and M4'

The mirrors M4 and M4' are ellipsoidal and defined by the drawings in Figure 4-69, from [8], p. 31.

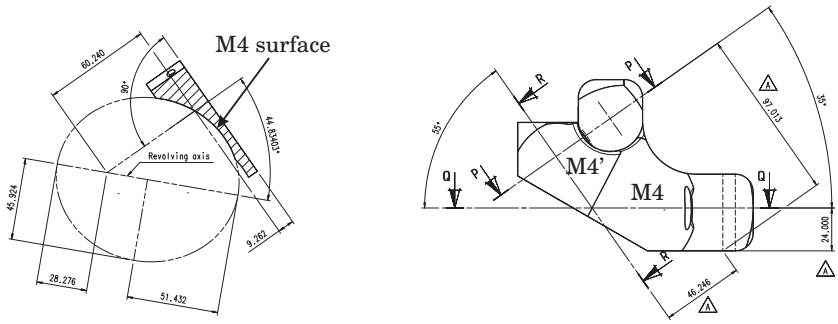

Figure 4-69 Band 9, M4 and M4' geometry

The values for the half axes a and b in Table 4-2, p. 14 in [8] are not fully in agreement with the drawing,

$$\begin{aligned} a_{drawing} &= 51.432 \text{ mm} \\ a_{table} &= 51.2266 \text{ mm} \\ b_{drawing} &= 45.924 \text{ mm} \\ b_{table} &= 45.7411 \text{ mm} \end{aligned}$$

but the values on the drawing are assumed to be the most accurate and will be used in the following calculations. The rim shapes are found numerically by measuring data points on the drawing.

4.9.3 Geometry of mirror M3

M3 is an ellipsoidal mirror defined by the drawings in Figure 4-70, from [8], p. 33.

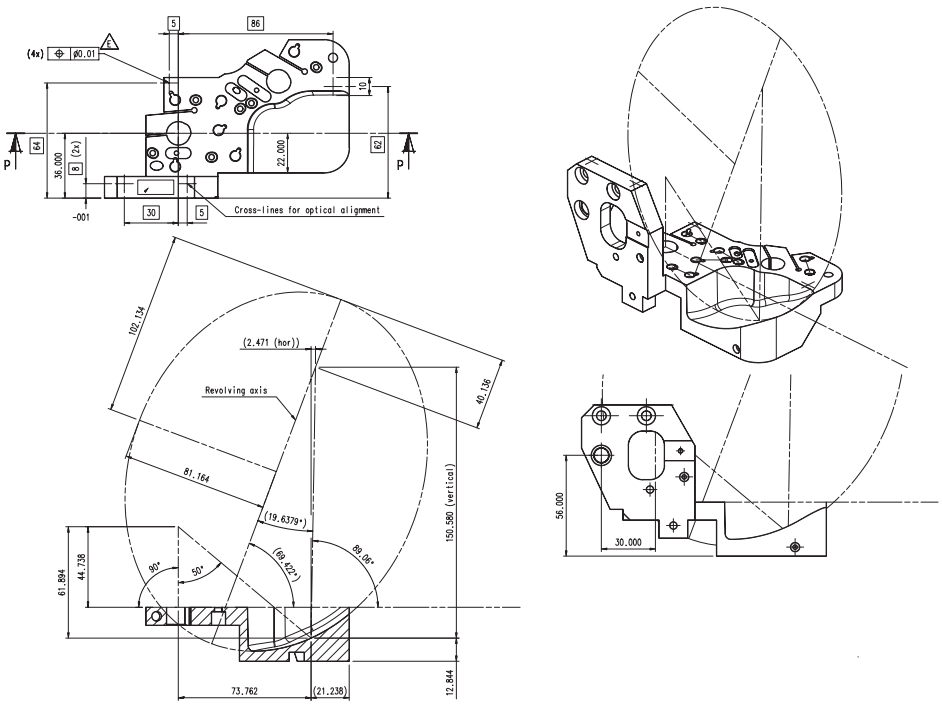

Figure 4-70 Band 9, M3 geometry

The values for the half axes a and b in Table 4-2, p. 14 in [8] and the distance between M3 and M4 are not fully in agreement with the drawing,

$$\begin{aligned} a_{drawing} &= 102.134 \text{ mm} \\ a_{table} &= 101.727 \text{ mm} \\ b_{drawing} &= 81.164 \text{ mm} \\ b_{table} &= 80.8407 \text{ mm} \end{aligned}$$

Also, the distance between M3 and M4 can be computed from the drawing as $d_{M3-M4} = 73.762/sin(50°) = 96.2895$ mm, whereas it is given as $d_{M3-M4} = D2 + D3 = 95.906$ mm in Table 4-1, p. 13 in [8] and as $d_{M3-M4} = d2 = 95.90$ mm in Table 16, p. 51 in [1]. In the following GRASP analysis it is assumed that the drawings contain the correct data. The rim shape are found numerically by measuring data points on the drawing.

4.9.4 Polarisation grid

A polarisation grid is located on the beam path between M4 and M3 in the distance 50.00 mm from M3 according to Table 4-1, p. 13 in [8]. In the same report on p. 46 a drawing gives the dimensions and grid parameters, see Figure 4-71

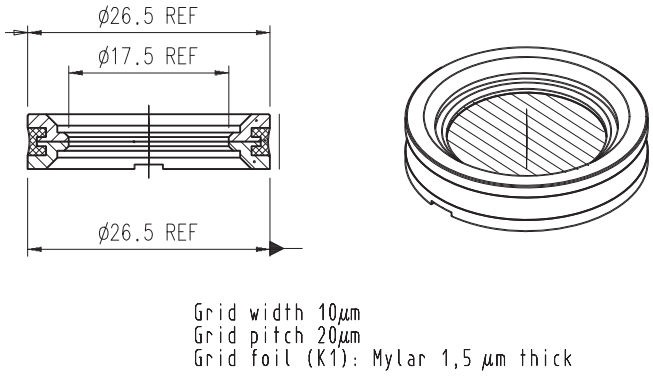

Figure 4-71 Band 9, polarisation grid.

4.9.5 Beam splitters

A beam splitter is located in front of each of the feeds to allow coupling of a LO-signal into the beam. The dimensions are given in Figure 4-72, from [8], p. 43 and the position is defined in [8], Table 4-4, p. 15 as 28 mm above the apex of the horn. In the GRASP analysis the beam splitters are treated as apertures without any dielectric material so that only the truncation effect is calculated.

4.9.6 Cryostat window and filter geometry

According to Table 3, p. 20 in [1] the cryostat window is located 44 mm above the nominal output waist position of the front-end system at 661 GHz. The information in Table 2 [1] (as summarized below in Table 4.10 then defines the position and diameters of the window and filters. In the GRASP analysis the filters and window are treated as apertures without any dielectric material.

The complete set-up of mirrors and windows is showin in Figure 4-73.

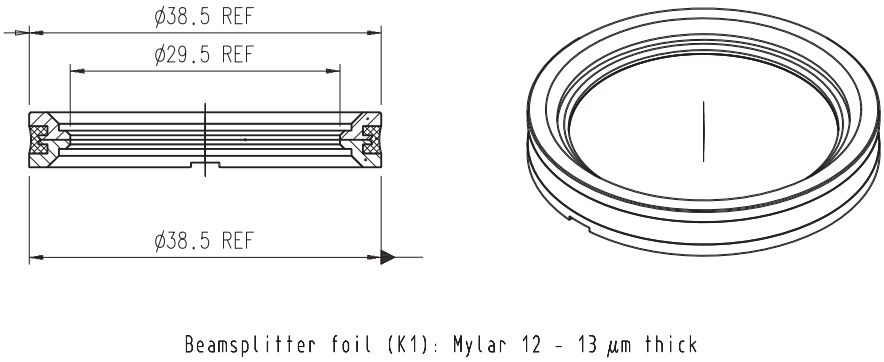

Figure 4-72 Band 9, beam splitter.

	Cryostat window	110K filter	15K filter
z-coordinate	0	49	81
diameter	20	25	30

Table 4.10 Band 9 cryostat window and filters. z-coordinate and diameter (in mm).

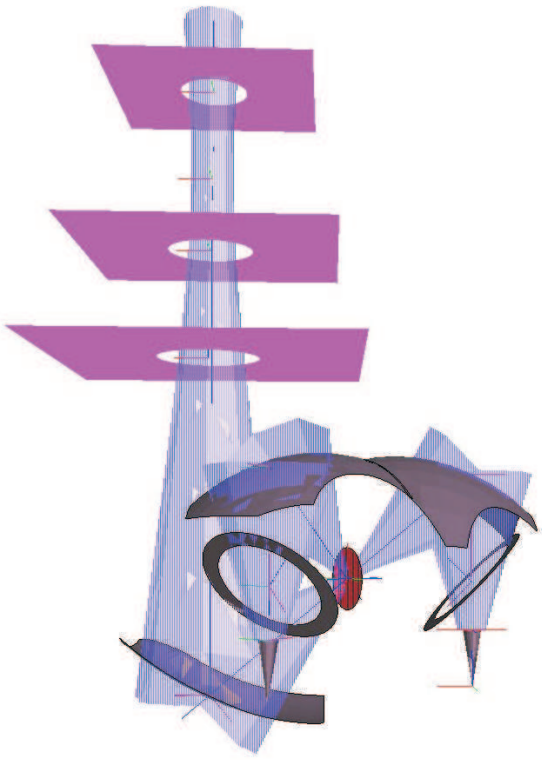

Figure 4-73 Band 9 geometry with mirrors, filters and cryostat window

4.9.7 GRASP analysis results

In Figure 4-74 the far field from the front end is computed without taking into account the filter and window apertures. Beams for the branch transmitted through the grid is compared to the ideal Gaussian beam which has a waist radius of $w_0 = 2.73$ mm at 661 GHz.

As for the other bands there is a loss in peak gain due to a different beam shape and due to sidelobes and power loss through the system, see Table 4.11 below.

	Relative incident power Transmitted branch	Relative incident power Reflected branch
Beam splitter	0.9988	0.9988
M4	0.9987	0.9984
Polarisation grid	0.9986	0.9983
M3	0.9768	0.9777
15K filter	0.9767	0.9777
110K filter	0.9766	0.9775
Cryostat Window	0.9757	0.9767

Table 4.11 Power loss through apertures and mirrors. Dielectric reflection loss is not included for the apertures and beam splitters.

It is seen that the major part of the loss, app. 2%, occurs at M3.

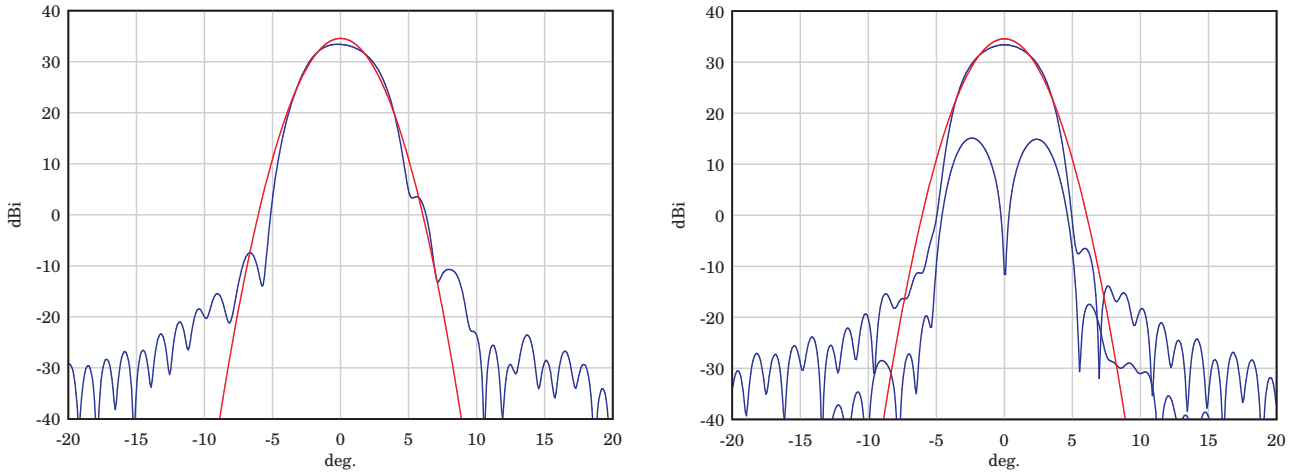

Figure 4-74 Far-field beams for mirror system with hybrid mode feed (blue curves) and ideal Gaussian output beam (red curves). Beam transmitted through the grid.
Left figure: $\phi = 0°$. Right figure: $\phi = 90°$.
Frequency: 661 GHz

Far-field cuts with and without filter and cryostat apertures are shown in Figure 4-75, and a comparison between the branch transmitted through the grid and the branch reflected in the grid is shown in Figure 4-76. It is seen that the apertures and cryostat windows have very little effect and that both branches have high cross polar field at a level app. 18 dB below the copolar peak. In the analysis it is important to use a plane-wave expansion of the incident field on the grid since the grid is located close to a waist, where the field has a significant radial component. A local plane wave assumption is not sufficiently accurate and instead the equivalent currents on the grid must be computed separately for each of the plane waves in the expansion. The front-end system has high cross polar field even though the mirror system is designed such that most of the cross polar generated by M1 will be compensated by M2. The problem is that the grid removes the cross polar field generated by M1 which should have been used to compensate the cross polar field generated by M2. A preliminary investigation has been carried out to test if a Dragone grid with slightly curved strips could be designed to reduce the cross polar level, but it seems not possible. The reason is that the Gaussian beam modes that represent the cross polar field are $90°$ out of phase with the co-polar mode so that the currents required on the grid for compensation of cross polarisation should have some amount of elliptical polarisation, which is not possible for a grid. A comparison of the system with and without the grid is shown on Figure 4-77 and it is seen that the grid increases the cross polar peak by app. 14 dB.

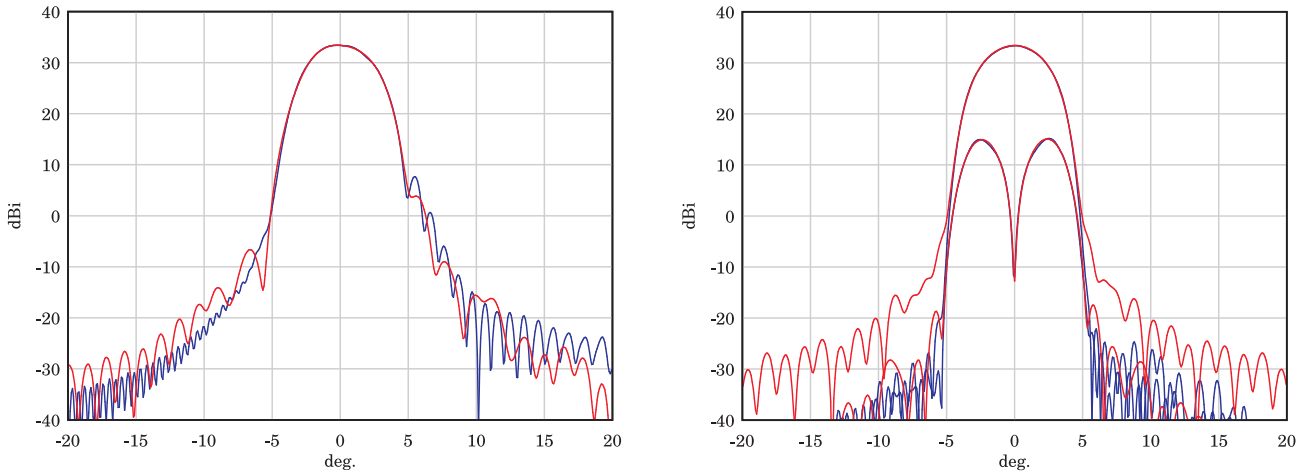

Figure 4-75 Far-field beams for mirror system without apertures (blue curves) and with apertures (red curves). Beam transmitted through the grid. Left figure: $\phi = 0°$. Right figure: $\phi = 90°$. Frequency: 661 GHz

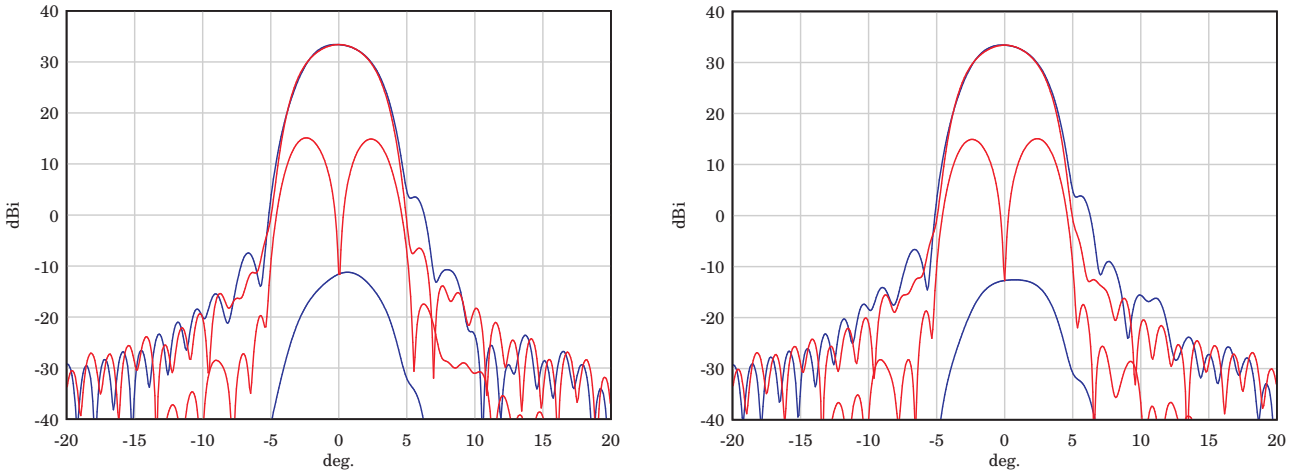

Figure 4-76 Far-field beams for the two polarisation branches, apertures included.
Left figure: Beam transmitted through grid.
Right figure: Beam reflected in grid.
Blue curves: $\phi = 0°$. Red curves: $\phi = 90°$.
Frequency: 661 GHz

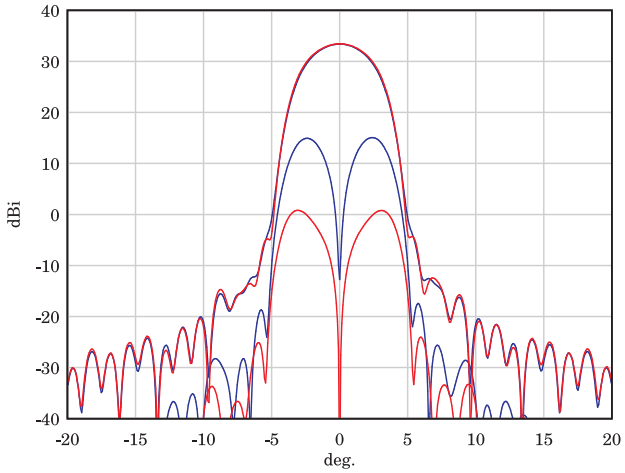

Figure 4-77 Far-field beams for mirror system with grid (blue curves) and without grid (red curves).
$\phi = 90°$ for all curves.
Frequency: 661 GHz

4.9.8 Band 9 summary

- The data in [8] with regards to the ellipsoidal mirror parameters are not fully consistent with the drawings.
- A loss of power of app. 2% occurs at M3.
- High cross polar field due to the polarisation grid.

4.10 Band 10

The design of the Band 10 sub-system is is described in [13], and the basic components are a corrugated horn and an ellipsoidal mirror. In addition, the system includes a polarization beam-splitter and local oscillator couplers. A schematic drawing is shown in Figure 4-78 and a 3D-drwaing in Figure 4-79.

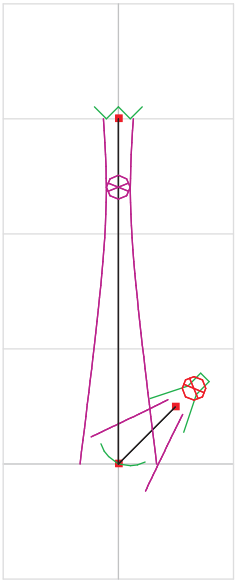

Figure 4-78 Schematic drawing of Band 10. A beam of width $5w$ is shown, corresponding to $-54.3dB$. Grid spacing $= 50mm$

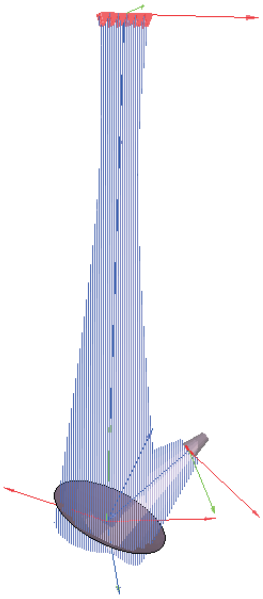

Figure 4-79 3D drawing of Band 10 at 868 GHz. A beam of radius $5w$ is shown, corresponding to $-54.3dB$.

A detailed analysis would require information about the mirror shape and rim and the polarization beam splitter. Due to lack of information, band 10 will not be treated further in this report.

4.11 Windows and filters

In Table 4.12 below, a summary is given for the cryostat window and filter transmission losses. The data are measurement results taken from [14] for all avialable bands.

Frequency	Band	Window	110K filter	15K filter	Report reference
84 GHz	3	0.2%	0.1%	0.1%	Figure 1, p.5
100 GHz	3	0.7%	2.2%	2.2%	Figure 1, p.5
116 GHz	3	1.2%	0.7%	0.7%	Figure 1, p.5
125 GHz	4	$\leq 0.3\%$	$\leq 1\%$	$\leq 1\%$	p.7
144 GHz	4	$\leq 0.3\%$	$\leq 1\%$	$\leq 1\%$	p.7
163 GHz	4	$\leq 0.3\%$	$\leq 1\%$	$\leq 1\%$	p.7
211 GHz	6	1.4%	1.4%	1.4%	p.13
243 GHz	6	1.2%	1.6%	1.6%	p.13
275 GHz	6	1.6%	2.5%	2.5%	p.13
275 GHz	7	2%			Figure 5, p.24
324 GHz	7	1%			Figure 5, p.24
373 GHz	7	2%			Figure 5, p.24
385 GHz	8		2.5%	4%	Figure 7, p.27
442 GHz	8		1%	3%	Figure 7, p.27
500 GHz	8		0.5%	2%	Figure 7, p.27
602 GHz	9	3%			Figure 9, p.29
661 GHz	9	3%			Figure 9, p.29
720 GHz	9	3%			Figure 9, p.29

Table 4.12 Transmission loss for windows and filters, from [14]

As indicated in the table, no data is available for the filters in band 7 and 9 and for the windows in band 8.

References

[1] M. Carter, “ALMA Front-end Optics Design Report”, Tech. Rep. FEND-40.02.00.00-035-B-REP Draft, ALMA, 2006-12-12.
1, 2, 6, 9, 11, 12, 14, 20, 21, 23, 26, 31, 35, 38, 42, 44, 45, 46, 54, 57

[2] M. Carter, R. Nesti, “ALMA Front-end Optics Design Report, Appendix 1”, Tech. Rep. FEND-40.02.00.00-035-B-REP, IRAM, 2007-02-14, First Version.
1, 3

[3] M. Carter, R. Nesti, “ALMA Front-end Optics Design Report, Appendix 2”, Tech. Rep. FEND-40.02.00.00-035-B-REP, IRAM, 2007-02-14, First Version.
1, 4

[4] M. Carter, F. Coq, A. L. Fontana, F. Tercero, J. A. Lopez Fernandez, C. Y. Tham, D. Erickson, “ALMA Front-end Optics Design Report, Appendix 3”, Tech. Rep. FEND-40.02.00.00-035-B-REP, IRAM, 2006-11-22, Draft.
1, 7, 8, 9, 11, 12, 16, 17, 18, 20

[5] S. Asayama, H. Iwashita, M. Sugimoto, “ALMA Front-end Optics Design Report, Appendix 4”, Tech. Rep. FEND-40.02.00.00-035-B-REP, NAOJ, 2007-01-29, Draft.
1, 22, 23, 24, 26

[6] M. Carter, F. Coq, B. Lazareff, “ALMA Front-end Optics Design Report, Appendix 6”, Tech. Rep. FEND-40.02.00.00-035-B-REP, IRAM, 2007-01-22, First Version.
1, 31, 32, 34, 39, 42

[7] M. Carter, P. Serre, F. Coq, S. Mahieu, A. L. Fontana, D. Maier, “ALMA Front-end Optics Design Report, Appendix 7”, Tech. Rep. FEND-40.02.00.00-035-B-REP, IRAM, 2006-12-12, First Version.
1, 43, 44, 45, 51

[8] M. Candotti, “ALMA Front-end Optics Design Report, Appendix 9”, Tech. Rep. FEND-40.02.00.00-035-B-REP, NOVA/SRON/NUIM, 2006-12-01, First Version.
1, 46, 54, 55, 56, 57, 62

[9] R. Johnson and H. Jasik, “Antenna engineering handbook”, McGraw-Hill, 1984.
9

[10] A.L. Fontana, M. Carter, B. Lazareff, F. Coq, “ALMA Band 3 Horn: Final Report”, Tech. rep., IRAM, 2004-10.

10, 11

[11] ESO, “Table 2: ALMA Cartridge, WVR, Windows and IR-filters mechanical information”, Tech. Rep. Table2 Window and IR FILTERS.pdf, ESO, 2007.
12, 23, 35

[12] J. Lesurf, “Millimetre-wave optics, devices and systems”, Adam Hilger, 1990.
31

[13] M. Candotti, M. Matsunaga, Y. Uzawa, “ALMA Front-end Optics Design Report, Appendix 10”, Tech. Rep. FEND-40.02.00.00-035-B-REP, NAOJ, 2007-07-04, First Version.
63

[14] M. Carter, A. L. Fontana, F. Mattiocco, B. Lazareff, K. Hara, M. Sugimoto, “ALMA Front-end Optics Design Report, Appendix 11”, Tech. Rep. FEND-40.02.00.00-035-B-REP, IRAM/NAJO, 2006-10-24, First Version.
65